IASSNS-AST-92-4

Fermilab Library
0 1160 0009321 5

Dup

Astrophysics Preprint Series

IASSNS-AST 92/4

On Spitzer's Mass Stratification Instability

Piet Hut and Yueming Xu

Institute for Advanced Study, Princeton, NJ 08540

Submitted to: ***Astrophysical Journal***

INSTITUTE FOR ADVANCED STUDY
OLDEN LANE
PRINCETON, NEW JERSEY 08540

On Spitzer's Mass Stratification Instability

Piet Hut and Yueming Xu

Institute for Advanced Study

Princeton, NJ 08540, U.S.A.

Abstract

We have studied a model star cluster enclosed in a spherical container with reflecting walls. The stars form a mixture of two species with one free parameter, the ratio of the stellar masses of the two species. With this parameter fixed, there are two other dimensionless free parameters which can be varied in order to perform thought experiments in a laboratory containing bottled star clusters. These two parameters can be chosen from a large number of candidates, such as the total energy and temperature (in units of their Jeans values), the density contrast between center and edge, the ratio of core radius and container radius, or the ratio of total masses in both species. In a space spanned by three or more of these parameters, the two-parameter family of solutions of isothermal equilibrium takes on highly complicated shapes, often leading to multivalued constraints on their projections, as we illustrate with a number of examples of special interest.

Although less realistic than Spitzer's analysis of his mass stratification instability in an open system, our model has the advantage of not involving any approximation. Our main results are: 1) a thermodynamic discussion of the series of equilibria which can be attained; 2) a quantitative verification of the range of validity of Spitzer's analytic approximations; 3) an interpretation for the series of equilibria in Spitzer's analysis, with a determination of the limits to their physical realization.

1. INTRODUCTION

Two-body relaxation is the dominant internal mechanisms driving the evolution of a star cluster. It is caused by the cumulative effects of many two-body encounters, most of them wide and therefore weak. In the limit in which all stars have equal mass, relaxation tends to drive the stellar velocity distribution function towards a Maxwellian. This goal, however, is unattainable since the stars in the high-velocity tail escape from the cluster. The resultant leak prevents the cluster from ever establishing equilibrium, and the resultant heat loss leads to a contraction of the central parts of the cluster. After the density contrast between center and halo has increased sufficiently, the negative heat capacity of self-gravitating systems causes the contraction to become unstable on a central relaxation time scale, much shorter than the half-mass relaxation time scale. This gravothermal catastrophe would result in the attainment of an infinite central density in a finite time, if two-body relaxation was the only mechanism. In reality, a variety of other physical processes will prevent such an unphysical singularity to be reached. For recent reviews, see Spitzer (1987), Binney and Tremaine (1987), Hut (1991).

In the more realistic case, in which stars can have a range of individual masses, the evolutionary picture becomes more complicated. Before escape can significantly affect the structure of the star cluster, mass segregation begins to dominate the initial phases of the evolution. If the stars are born with comparable velocities, as seems likely from a common origin in molecular clouds, they are initially distributed in a similar way throughout the cluster. However, in the attempt to reach equipartition of energy, the more massive stars tend toward lower velocities, which causes them to drift toward the center of the cluster. The increased central density in due time then leads to the onset of the gravothermal catastrophe.

The simpler problem, in which stars have equal masses, has been studied in great detail in a variety of analytical and numerical approximations, as well as through a variety of simulations. The more realistic problem in which stars have a realistic mass spectrum, in contrast has received much less attention since it is much less amenable to analytic approximations. However, now that large-scale simulations are becoming increasingly detailed (*cf.* Hut 1991 and references therein), the problem of understanding the underlying basic physical processes, such as mass segregation, is becoming more acute. With this motivation, we have re-investigated the analytic treatment given by Spitzer (1969). His discovery of the mass stratification instability, in the simplest case in which stars come in only two species, has been the most important contribution to our basic understanding of mass segregation. It has been our goal to shed more light on the character of the approximations he used, as well as to give an overall description of the behavior of a general two-mass system.

1.1. Construction of Equal Mass Models

When all stars are given equal mass, it is possible to build many elegant equilibrium models for the simplest type of star clusters, which are spherically symmetric, and isotropic in their velocity distribution. For a star cluster, an equilibrium model is defined as a model

which is in equilibrium on a dynamical time scale, and only evolves slowly on a time scale of two-body relaxation. In spherical isotropic models, the stars have a phase space density in the form of a one-dimensional distribution function $f(E)$, dependent only on the energy of the stars (see Binney and Tremaine 1987 for a recent discussion of star cluster models).

Spherical isotropic models are relatively easy to construct numerically. Examples are the one-parameter families of polytropes and King models. There are even several analytical solutions known, where we define a model as analytical if we can write the potential and density explicitly as a function of the radius, and in addition the distribution function as an explicit function of the energy. If we allow infinite mass, and in addition a centrally diverging density, the simplest analytical model is the singular isothermal sphere.

Requiring a finite total mass, and finite central density, we have two classes of solutions, for finite and infinite radial extent. An example in the first class is the polytrope with polytropic index $n = 1$, discovered by Ritter (*cf.* Chandrasekhar 1939). Examples with a non-zero density out to infinity are: the polytrope with polytropic index $n = 5$, discovered independently by Schuster and Emden and called the Plummer model (*cf.* Chandrasekhar 1939); and the isochrone model discovered by Hénon (1960). Interestingly, both of these models were recovered as members of a single family of analytical models by Dejonghe (1984), together with a third member, described in his eq. (31). In addition, he presents a whole series of other analytical models in the form of a one-parameter family, as described in his eq. (36) [Note that our 'analytical models' are called 'complete analytical models' in his terminology].

Requiring a finite total mass, but allowing infinite central density, while excluding a central mass singularity (no 'black hole'), we can call Jaffe's (1983) model analytical, if we allow Dawson's integral into the class of 'known' function. More recently, an analytical model resembling Jaffe's, but with a simpler distribution function, was given by Hernquist (1990).

1.2. Stability and Evolution of Equal Mass Models

On a relaxation time, all star clusters are unstable. While two-body encounters attempt to establish an isothermal distribution function, this attempt is thwarted by unavailability of the high-energy tail of a Maxwellian velocity distribution: stars moving faster than the escape velocity will leave the system. The presence of a tidal galactic field will speed up the escape process, by lowering the potential barrier. In addition, tidal shocking by passing molecular clouds (for galactic clusters) or passages through the disk or near the galactic bulge (for globular clusters) will lower the lifetime of star clusters. Recent discussions of the evolution of the galactic globular cluster population, which include environmental effects of the galaxy, are given by Aguilar, Hut & Ostriker (1988), and Chernoff & Weinberg (1990).

In the context of our present paper, we will concentrate on the idealized problem of an isolated star cluster in which all stars can be treated as point masses. We refer to the clear and concise monograph by Spitzer (1987) for a general introduction to the subject of dynamical evolution of star clusters. Another recent introduction can be found in Ch. 8 of Binney and Tremaine (1987). For a short review of globular cluster dynamics, see

Elson *et al.* (1987). Here we will just mention a few of the salient points of the evolution of an idealized cluster model, consisting of a self-gravitating collection of point masses all of which have the same mass. For a more complete overview of the literature, we refer the reader to the above three references.

As a result of the escape mechanism, the outer regions of such a star cluster, where the escape velocity is lower, will have a lower effective temperature. Two-body relaxation will respond with a heat flow from the inner regions outward. This loss of energy causes the central regions to contract, and as a result the temperature will increase. The latter effect is a consequence of the virial theorem, applied to the inner area. Such an application is valid, even though the virial theorem is a global relation valid for the system as a whole, since the inner regions have a much smaller relaxation time than the outer area. This implies that we can regard the outer area as approximately frozen on the time scale of evolution of the central part of a star cluster. When the increase in temperature in the central regions is higher than the increase in the surrounding regions, the contraction will accelerate.

The instability of the inner dense regions of a star cluster can be studied in an idealized thought experiment by placing the inner regions in a spherical container. The walls of the container reflect the outgoing stars back in again, but the mass and therefore the gravity of the container wall is neglected. An even simpler model for such a system can be obtained if we replaced the stars by an ideal gas. Antonov (1962) analyzed such a self-gravitating isothermal ideal gas, surrounded by a fixed spherical adiabatic wall. He found that this system was stable as long as the central density $\rho(0)$ was not too high, compared to the density near the edge of the container, $\rho(R)$, where R, the radius of the boundary. In that case, any small perturbation in the heat distribution throughout the system would decay, and the system would return to the original isothermal state. However, he found that there exists a critical value for the central density, $\rho_{cr}(0) = 709\rho(R)$. For $\rho(0) > \rho_{cr}(0)$, the system is linear unstable against perturbations, and a small initial heat flow outwards from the center will caused an increasingly rapid contraction.

Antonov's instability was studied in more detail, and illustrated with many physical considerations and different types of thought experiments by Lynden-Bell & Wood (1968). They introduced the term 'gravothermal catastrophe' for the ever-accelerating contraction of the inner regions, leading to a gravitational collapse. Inagaki (1980) and Ipser & Kandrup (1980) showed that the instability criterion derived by Antonov for a gas sphere also holds for a stellar dynamical system. Cohn (1980) performed a numerical simulation in which he followed the evolution of a star cluster in a Fokker-Planck approximation. He convincingly showed the operation of the gravothermal catastrophe, leading to a self-similar contraction in the late stages of the collapse. A detailed analysis of the self-similar contraction in a gas sphere model was given by Lynden-Bell & Eggleton. Recently, Makino and Hut (1991) studied the detailed behavior of the collapse of the core in a linear stability analysis of a gas sphere for different types of heat conduction.

1.3. Two-Mass Models

No analytic models have yet been constructed for any genuine two-mass model, or

any other set of several masses or of a continuum mass distribution. Of course, trivial models can be found easily by taking any equal-mass model, and interpreting an arbitrary fraction of the mass density as being made up of particles which have different masses but which all share the exact same velocity distribution. But beyond this, it would be highly desirable to have non-trivial models, either for an isothermal equilibrium between two or more mass species, or for any other non-trivial set of velocity distributions.

Numerical models can be constructed rather easily, by taking the prescription for the distribution function of an equal-mass model, and generalizing it in some straightforward way to apply to several mass groups. Poisson's equation now has to be solved for the simultaneous presence of all these mass groups, which together determine the run of the cluster potential. One often-used example is that of multi-mass King models, in which each species is assigned the same (pseudo-)temperature (King 1989, Pryor *et al.* 1989).

The dynamical evolution of multi-mass systems is complicated, and cannot be approximated by a series of thermal equilibrium models. Starting from initial conditions in which all stars are drawn from the same velocity distribution, the more massive stars do tend to slow down, but at the same time they tend to aggregate in the collapsing core which then decouples thermally from the rest of the system while undergoing a modest local rise in temperature. For reviews, and references to the literature, see Spitzer (1987) and Hut (1991).

1.4. Our Approach

In this paper we aim at a deeper understanding of Spitzer's mass stratification instability. To do so, we truncate our star cluster by imposing a rigid boundary at a finite radius. Stars simply bounce off from this adiabatic wall, which allows neither stars nor heat to leak out. While this prescription is of course artificial, it has two great advantages: it allows the system to remain in equilibrium, and it allows us to solve numerically for all thermodynamic variables to arbitrary accuracy.

In §2 we briefly discuss the analogous situation of an equal-mass system enclosed within an adiabatic wall, before extending the description to a two-mass system. We then graphically illustrate the two-parameter family of equilibrium distribution, in order to get some insight in the complex and non-linear relationships between the different extensive and intensive thermodynamic variables. Our work extends earlier investigations of general two-component isothermal spheres by Taff *et al.* (1975), and of enclosed two-component isothermal spheres by Saito & Yoshizawa (1975), Lightman (1977), and Yoshizawa *et al.* (1978). An alternative approach to the construction of finite two-mass models is to drop the requirement of strict isothermality, by introducing lowered Maxwellian distributions. One example of such approach is the construction of King models, mentioned above. Merritt (1981) showed that in this way counterexamples to Spitzer's mass stratification instability could be found, but he also pointed out that they do not apply to realistic stellar systems, a point which was further clarified by Katz & Taff (1983).

In §3 we first discuss the different approximations made in Spitzer's (1969) approach. We then compare this results with the analogue situation in our bounded models. In order to highlight the main qualitative features, we introduce a toy model in which the density

is very much simplified. Using this model, we show the physical interpretation of the different regimes discussed in Spitzer's approach. Specifically, we discuss which fraction of his parameter regime can be realized. In §4 we sum up, and discuss our results.

2. TWO-MASS MODELS IN A REFLECTING CONTAINER

2.1. *The Equal-Mass Case*

Before we discuss the general multi-mass case, let us briefly review the equal-mass case. When we solve Poisson's equation for an isothermal, self-gravitating ideal gas, we find a dependence of density on radius as plotted in Fig. 1 (a more detailed discussion will be given in §2.2). Looking at the shape of the figure, there is essentially only one isothermal sphere, apart from scaling in mass and radius. But when we enclose our system in a spherical container, we introduce a new scale length, in the form of the radius R of the container, besides the core radius r_c. As a result, we obtain a one-parameter family of physical solutions, the properties of which were studied in great detail by Lynden-Bell & Wood (1968).

In Fig. 1, the core radius is defined as

$$r_c = \sqrt{\frac{9}{4\pi G\rho(0)\beta}}, \tag{1}$$

where β is defined as a measure for the inverse temperature:

$$\beta = \frac{m}{kT}. \tag{2}$$

In these equations, G is the gravitational constant, $\rho(0)$ is the central density, m is the mass of an individual particle, k is Boltzmann's constant, and T is the temperature of the system. For further motivation for these definition, see the more detailed discussion following Eqs. (4, 10).

In Fig. 2 we present this family of solutions in an energy-temperature diagram, following the approach of Binney & Tremaine (1987). The quantities plotted along the axes are made dimensionless, through the addition of the proper powers of M, the total mass of the system (the mass of the walls is neglected). The total energy of the system is denoted by E. In astrophysical terms, we have plotted the energy and temperature in units corresponding roughly to the Jeans energy and the Jeans temperature. In these units, energies or temperatures much larger than unity imply that the system approaches an isothermal gas, for which self-gravity is unimportant. An example is provided by point A in Fig. 2, for which $E \simeq \frac{3}{2}\frac{M}{m}kT$.

In Fig. 1 the left-most vertical line corresponds to the position of the confining sphere which corresponds to this near-ideal-gas point A. The radius of the wall is less than a core

radius, and therefore the density contrast between center and edge of the gas distribution is less than a factor three. When we move the confining wall out to larger radii, for example to position B in Fig. 1, the density contrast increases significantly. This is a clear sign that self-gravity has now become important. Indeed, the corresponding point in Fig. 2 indicates a negative energy, which implies that the total gravitational potential energy exceeds the kinetic energy in magnitude. Moving the wall out further in Fig. 1, to points C and D causes the system to move correspondingly along the curve in Fig. 2, ultimately reaching the center of the spiral when the wall recedes to infinite distance.

The spiraling behavior in Fig. 2 of the series of isothermal equilibria, which appears for large density contrasts within our container, is a consequence of the slightly wavy character of the run of the density in Fig. 1. The latter in turn is a consequence of the nature of Poisson's equation, being a second-order differential equation (see Chandrasekar 1939 for a detailed analysis of this behavior). In order to highlight the essential qualitative characteristics of the isothermal sphere, we present in Appendix A a toy-model in which the spiraling behavior is absent, while the property of a negative heat-capacity (see below) is maintained. The results of this toy-model are plotted in Fig. 3.

There are many interesting thermodynamic thought experiments which one can perform, when one views the enclosing sphere as a black box, or better a black bottle, containing initially an equilibrium isothermal sphere. One can picture the sphere to be filled either with an ideal gas or with a stellar dynamical system of stars. Apart from the need of a somewhat larger container (and a larger lab) in the second case, the physics is the same, as long as all changes in external parameters are made on timescales which are very long with respect to the internal relaxation time scales.

One set of experiments could be done by placing the bottle in a heat bath, corresponding to the statistical description of a canonical ensemble. Specifying the temperature in Fig. 2, the energy could then be read off from the graph. The part of the curve descending past A would be stable, up to the point B. No isothermal equilibria would be available for lower temperatures, and the system would undergo core collapse.

Alternatively, one could use an adiabatic wall, corresponding to the statistical description of a microcanonical ensemble. Here once could descend through a series of equilibrium states, while changing the total energy in small decrements at each step. In this case the temperature would be the dependent variable. Stability will be insured until we reach the point C, below which no isothermal equilibrium with lower energy can be found (Antonov 1962). At this point we would again encounter core collapse. Note that the heat capacity of the system as a whole has become negative along the trajectory BA. For more details, and a host of other thought experiments, see Lynden-Bell & Wood (1968). We now proceed to the more general case in which we allow different species of particles to be present, each with a different particle mass.

2.2. The Multi-Mass Case

Let us again take a isothermal, spherically symmetric distribution of stars, enclosed in a reflecting spherical wall, with radius R. At first we will choose R very large, much larger than the region under consideration. And since we will only study equilibrium situations

in the present paper, we can replace our stellar dynamical system by that of an ideal gas. In the following we will summarize the most important expressions describing the various equilibrium states. For more details, we refer the reader to Binney & Tremaine (1987) and Spitzer (1987), as well as to previous papers on two-mass models (e. g. , Taff *et al.* 1975, Saito & Yoshizawa 1976, Lightman 1977, Yoshizawa *et al.* 1987).

To start with, let us take a general multi-mass system, with N different types of stars, so that each star has a mass m_i, with $m_1 < m_2 < \ldots < m_N$. All stars are drawn from distributions sharing the same temperature T. The mass density $\rho_i(r)$ of star of type i as a function of radius r depends on the gravitational potential $\psi(r)$ as

$$\rho_i(r) = \xi_i\, \rho(0) \exp[-\beta_i\, \psi(r)]. \tag{3}$$

Here we have introduced a measure β_i for the inverse temperature:

$$\beta_i = \frac{m_i}{kT}. \tag{4}$$

The central density $\rho_i(0)$ is expressed as a fraction ξ_i of the total density:

$$\rho_i = \xi_i \rho(0), \tag{5}$$

which implies $\sum_i \xi_i = 1$.

The gravitational potential can be written as the sum of contributions from the individual mass components:

$$\psi(r) = \sum_i \psi_i(r), \tag{6}$$

where each contribution satisfies Poisson's equation

$$\frac{1}{r^2}\frac{d}{dr}\left(r^2 \frac{d\psi_i}{dr}\right) = 4\pi G \rho_i(r), \tag{7}$$

with G denoting the gravitational constant. Eq. (7) must have as a boundary condition $\psi_i'(0) \equiv d\psi_i/dr = 0$, based on symmetry. In addition we will choose as a gauge the extra boundary condition $\psi_i(0) = 0$. Thus $\psi(r)$ measures the height of the potential well as measured from the bottom, and $\psi_i(r)$ measures the separate contribution from stars of type i.

The mass of all the stars of type i, enclosed within radius r, follows from integrating Eq. (7) as

$$M_i(r) = 4\pi \int_0^r \rho_i(\tilde{r})\, \tilde{r}^2\, d\tilde{r} = \frac{r^2}{G}\psi_i'(r). \tag{8}$$

We will now rewrite Poisson's Eq. (7) in terms of dimensionless quantities. First we define a formal measure of inverse temperature

$$\beta = \sum_i m_i/kT. \tag{9}$$

This is done purely for mathematical convenience, since there is no physical significance to summing up the individual particle masses. If there is one type of star with a mass much larger than that of the other types, β measures mainly the contribution of that heaviest species of stars, $\beta \approx \beta_N$, even if the total mass M_i in all the stars of that type would be very small. Second, we introduce a scale length r_c as a measure of a core radius:

$$r_c = \sqrt{\frac{9}{4\pi G\rho(0)\beta}}, \tag{10}$$

in analogy with the King radius (*cf.* Binney & Tremaine 1987), to which this expression reduces in the limit $N = 1$.

We now switch to a dimensionless radius

$$x = r/r_c, \tag{11}$$

and a dimensionless potential

$$\phi(x) = \beta\psi(r). \tag{12}$$

Similarly, we can define the individual potential contributions to be

$$\phi_i(x) = \beta\psi_i(r), \tag{13}$$

which implies $\phi(x) = \sum_i \phi_i(x)$.

Finally, we can relate β to the individual measure of inverse temperature β_i by introducing another formal measure of relative mass

$$\mu_i = m_i / \sum_j m_j, \tag{14}$$

an expression which again only has a bookkeeping function, and no physical meaning. It is only given here to allow us to connect the individual masses with individual inverse temperatures:

$$\beta_i = \beta\mu_i. \tag{15}$$

In terms of the above quantities, the dimensionless version of Poisson's equation now reads:

$$\frac{1}{x^2}\frac{d}{dx}\left(x^2\frac{d\phi_i}{dx}\right) = 9\,\xi_i \exp[-\mu_i\,\phi(x)]. \tag{16}$$

2.3. The Two-Mass Case in the Limit $\mu_2 \gg \mu_1$ and $\xi_2 \gg \xi_1$

Consider a system with only two species of stars, which we will address as heavy and light stars. In addition, let the individual heavy stars be far more massive than the light ones, *i. e.* $\mu_2 \gg \mu_1$, or $\mu_2 \simeq 1$. Furthermore, let us start with the case in which the heavy

stars dominate the central mass density: $\rho_2(0) \gg \rho_1(0)$. In this extreme case, the halo of the heavy stars will still be contained within the core of the light stars. We can distinguish four different radial regimes: an inner core for the heavy stars, an inner halo region in which the heavy star density starts drop fast but still dominates the local mass density, an outer core region in which the local star density is dominated by the nearly constant density of the light stars, and an outer halo in which the light star density starts dropping fast as well.

To be more specific, let us introduce a measure for the core radii r_{ci} for the individual mass species:

$$r_{ci} \equiv \sqrt{\frac{9}{4\pi G\rho_i(0)\beta_i}}, \tag{17}$$

in analogy with Eq. (10). In addition, we will need an extra intermediate radius in the case that the heavy stars dominate the central density, to denote the radial position at which the local mass densities in the two species become comparable. As we will see below, in §2.3.3, a measure for this cross-over radius is given by the mixed expression

$$r_c \equiv \sqrt{\frac{9}{4\pi G\rho_1(0)\beta_2}}. \tag{18}$$

It is convenient to introduce an extra dimensionless parameter

$$y = r/r_{c1} \tag{19}$$

for measuring length in units which are taylored to the distribution of the lighter particles. The equivalent parameter for the heavy parameters to first approximation the same as our global parameter x defined just before Eq. (16): $r/r_{c2} \simeq r/r_c = x$.

Finally, for our two-mass system we can introduce a more compact notation for the mass ratio

$$\mu = \frac{m_2}{m_1} = \frac{\mu_2}{\mu_1}, \tag{20}$$

and the ratio of central densities

$$\xi = \frac{\rho_2(0)}{\rho_1(0)} = \frac{\xi_2}{\xi_1}. \tag{21}$$

To summarize, we list the two approximations we have made in our limiting case of interest, followed by some of their their consequences

$$\mu \simeq \frac{1}{\mu_1} \gg \mu_2 \simeq 1, \tag{22}$$

$$\xi \simeq \frac{1}{\xi_1} \gg \xi_2 \simeq 1, \tag{23}$$

$$\beta \simeq \beta_2 = \mu\beta_1 \gg \beta_1 \tag{24}$$

$$\rho(0) \simeq \rho_2(0) = \xi\rho_1(0) \gg \rho_1(0) \tag{25}$$

$$r_c \simeq r_{c2} = (\xi\mu)^{-1/2} r_{c1} \ll r_{c1}, \tag{26}$$

$$x \simeq (\xi\mu)^{1/2} y \gg y. \tag{27}$$

Finally, we have the following identity:

$$r_e = \xi^{1/2} r_{c2} = \mu^{-1/2} r_{c1}. \tag{28}$$

2.3.1 The regime $r < r_{c2}$

We are now ready to analyze the four regions. In the innermost region, the inner core, we have $\mu_1\,\phi(x) \ll \mu_2\,\phi(x) \ll 1$, and Eq. (16) gives us a good parabolic approximation for both potential contributions, while the densities in both species remain roughly constant:

$$\left.\begin{aligned} \phi_1(x) &\simeq \frac{3}{2}\frac{1}{\xi}x^2 \\ \phi_2(x) &\simeq \phi(x) \simeq \frac{3}{2}x^2 \\ \rho_1(x) &\simeq \rho_1(0) \\ \rho_2(x) &\simeq \rho_2(0) \simeq \rho(0) \end{aligned}\right\} \quad \text{for} \quad x \ll 1. \tag{29}$$

2.3.2 The regime $r_{c2} < r < r_e$

In the second region, the inner halo (of the heavy particles), the heavy stars shows the characteristic $\sim x^{-2}$ density drop-off of an isolated equal-mass isothermal sphere, with the associated logarithmic potential. Well outside the core radius of the heavy stars, the coefficients 9/2 given below follow directly from a substitution of a logarithmic potential in Eq. (16). Meanwhile, the density of the lighter stars remains roughly constant (for a analysis of the deviations from constant density, see §3). Therefore, the contribution of the light particles to the potential continues to raise quadratically. To sum up, in this regime we have $\mu_2\,\phi_1(x) \ll 1 \ll \mu_2\,\phi_2(x)$, which leads to:

$$\left.\begin{aligned} \phi_1(x) &\simeq \frac{3}{2}\frac{1}{\xi}x^2 \\ \phi_2(x) &\simeq \phi(x) \simeq \ln\left(\frac{9}{2}x^2\right) \\ \rho_1(x) &\simeq \rho_1(0) \\ \rho_2(x) &\simeq \frac{2}{9}\rho(0)\frac{1}{x^2} \end{aligned}\right\} \quad \text{for} \quad 1 \ll x \ll \sqrt{\xi}. \tag{30}$$

2.3.3 The regime $r_e < r < r_{c1}$

In the third region, the outer core (of the light particles), the density of the heavy particles drops off exponentially. A physical reason for the onset of this very steep drop in density is that the potential is dominated by the light stars, which in turn requires that $\rho_1(x)/\rho_2(x) \gg 1$. The mathematical reason can be seen from Eq. (16), where the suppression of the heavy stars by the light potential requires $\mu_2\,\phi_1(x) \gg 1$. The first condition results in $r \gg \sqrt{2}/3\,r_e$, while the second gives $r \gg \sqrt{2/3}\,r_e$.

Obviously, the difference of a factor of $\sqrt{3}$ between the two above expressions is irrelevant, and in any case we could have chosen other factors than unity in the two $\gg 1$ inequalities. Neglecting these factors, both criteria simply require $r \gg r_e$. We have used this freedom in the exact definition of r_e in such a way as to keep the analogy with the definitions of r_{c1} and r_{c2} as close as possible.

Meanwhile, the density and potential contribution of the lighter stars continue as before, but are now expressed in the more natural variable y rather than x. To sum up, we now have $\mu_1\,\phi_1(x) \ll 1 \ll \mu_2\,\phi_1(x)$, which leads to:

$$\left.\begin{aligned}
&\phi_1(y) \simeq \phi(y) \simeq \frac{3}{2}\,\mu\,y^2 \\
&\phi_2(y) \approx \ln\left(\frac{9}{2}\,\xi\right) \\
&\rho_1(y) \simeq \rho(y) \simeq \rho_1(0) \\
&\rho_2(y) \simeq \rho(0)\,\exp\left(-\frac{3}{2}\,\mu\,y^2\right)
\end{aligned}\right\} \quad \text{for} \quad \frac{1}{\sqrt{\mu}} \ll y \ll 1. \tag{31}$$

2.3.4 The regime $r > r_{c1}$

In the fourth region, the outer halo, the light particles now show the characteristic $\sim y^{-2}$ density drop-off of an isolated equal-mass isothermal sphere, with the associated logarithmic potential, and the same coefficients of 9/2 found before in §2.3.2. For the heavy particles, the previous exponential drop-off now changes into a power-law. The expression below is given here only for completeness, because the exponential cut-off factor, inherited from the previous regime, makes the contribution of the heavy stars outside the core of the lighter stars utterly negligible. To sum up, we have $\mu_1\,\phi_1(x) \gg 1$, and we get:

$$\left.\begin{aligned}
&\phi_1(y) \simeq \phi(y) \simeq \mu\,\ln\left(\frac{9}{2}y^2\right) \\
&\phi_2(y) \approx \ln\left(\frac{9}{2}\,\xi\right) \\
&\rho_1(y) \simeq \rho(y) \simeq \frac{2}{9}\,\rho_1(0)\,\frac{1}{y^2} \\
&\rho_2(y) \simeq \rho(0)\left(\frac{2}{9}\,\frac{1}{y^2}\right)^{\mu}
\end{aligned}\right\} \quad \text{for} \quad y \gg 1. \tag{32}$$

2.4. General Two-Component Models

Because of the rapid increase of the gravitational potential of the light particles, the density distribution of heavy particles has an effective cut-off at the radius of $r \approx r_e$. The total mass of the heavy particles can therefore be approximated by Eq. (8):

$$M_2 \approx \frac{r_e^2}{G}\,\psi_2'(r_e) = \frac{2\,r_e}{G\,\beta_2}. \tag{33}$$

This approximation is accurate to within 30%, for the whole range $\xi > 2$, as we determined from a comparison with direct numerical integration.

A natural scale with which to compare M_2 is the core mass of the light particles:

$$M_{c1} = \eta\frac{4\pi}{3}\,\rho_1(0)\,r_{c1}^3 = \eta\frac{3\,r_{c1}}{G\,\beta_1} \approx \frac{1.55\,r_{c1}}{G\,\beta_1}, \tag{34}$$

where the value of $\eta \approx 0.517$ follows from a numerical integration of the density profile of the regular isothermal sphere. Using this scale, we obtain the following dimensionless expression characterizing the total mass in heavy stars:

$$\frac{M_2}{M_{c1}} \approx \mu^{-3/2}, \tag{35}$$

when $\mu = \mu_2/\mu_1 \gg 1$ and $\xi = \xi_2/\xi_1 \gg 1$. In this expression we have neglected the numerical factor 1.3 on the right hand side, since the accuracy of Eq. (34) is of a comparable 30%, making the last digit not significant.

For each choice of stellar components, *i. e.* for each choice of the stellar mass ratio μ, we can integrate Eq. (16) to obtain the gravitational potential and the density profiles of two-component isothermal gas spheres. The only free parameter left is the ratio ξ of central densities. The results are plotted in Figs. 4 and 5. Fig. 4 shows the density profiles $\rho_i(r)$. The ratio μ between the heavy particle mass and the light particle mass was chosen to be 100, 10, 5, and 2 in Figs. a, b, c, and d, respectively.

Each of the panels in Fig. 4 is a superposition of six different models, each of which is characterized by a different value of ξ, the ratio of the central densities in the heavy and the light components. The short-dashed line applies to $\xi = 10^8$, the dotted line to $\xi = 10^6$, the short dash–dotted line to $\xi = 10^4$, the long-dashed line to $\xi = 10^2$, the solid line to $\xi = 1$, and the long dash–dotted line to $\xi = 10^{-2}$. For each ξ value, two lines are drawn, one each for the density $\rho_i(r)$ for the two components $i = 1, 2$. The densities are normalized with respect to the central density $\rho_1(0)$ in the light component. The radii are normalized with respect to the core radius r_{c1} of the light particles, defined formally in Eq. (17). As shown in Fig. 4a for $\mu = 100$, the density distribution of the light component is not noticeably affected by the presence of the heavy component, even for very high ξ values. Note also that the heavy particles are confined to a radius comparable to the cut-off radius $r_e = \mu^{-1/2} r_{c1} = 0.1\,r_{c1}$, as we derived in the analysis of §3.3.

The shape of the potential well $\phi_i(r)$ for the four different particle mass ratios is shown in Fig. 5. In each panel we have assumed a central density ratio of $\xi = 10$. The

full lines indicate the total potential $\phi(r)$, while the separate contributions of the light and the heavy particles is indicated by the dotted and dashed lines, respectively. The dotted lines are vertically shifted by the amount of $\phi_2(\infty)$. With this shifted representation, the total potential approaches that of the heavy particles for $r \to 0$ and that of the light particles for $r \to \infty$. Note that for large μ values the total potential is hardly affected by the presence of the heavy particles. For example, in Fig. 5a we can see that the parabolic approximation for the potential contribution of the lighter particles, which continues till $r/r_{c1} \sim 1$, will be nearly everywhere in the core far larger than the total contribution of the heavier particles (of order $\mu = 100$ at the lighter particle core radius, according to the analysis in §3.3).

2.5. A Spherical Container

The previous models have had infinite extent, and infinite total mass in the lighter component. We now proceed to finite models by imposing the constraint that we only investigate our models for radial values $r < R$. The physical interpretation of this cut-off value is that we consider the whole stellar system to be enclosed within an spherical container, *i. e.* a sphere with a perfectly reflecting wall.

2.5.1. The Virial Theorem

As we discuss in greater length in Appendix C, for each species i we can write a virial theorem as

$$\sum_j W_{ij}(R) = B_i(R) - 2K_i(R), \tag{36}$$

which relates the potential energy contribution at the left with the kinetic energy of the species i at the right. Here the boundary terms $B_i(R)$ is related to the boundary pressures $P_i(R)$ by

$$B_i(R) = 4\pi R^3 P_i(R) = 4\pi R^3 \frac{\rho_i(R)}{\beta_i}, \tag{37}$$

while the kinetic energy in each species i is given by

$$K_i(R) = \frac{3M_i(R)}{2\beta_i}. \tag{38}$$

The potential energy sum in Eq. (36) can be interpreted as the energy released during the infall of particles of species i, if we build up our system from the core outwards. Each term W_{ij} gives the contribution to this sum of one of the species j:

$$W_{ij}(R) = -4\pi G \int_0^R \rho_i(r)\, r\, M_j(r)\, dr \tag{39}$$

Note that for two different species, the total interaction energy between these two species, in the form of their contribution to the total binding energy of the whole system, is given by the sum $W_{ij} + W_{ji}$, although $W_{ij} \neq W_{ji}$ (see Appendix C, Eq. C17).

Adopting units in which $G = R = 1$ and using the Virial theorem (Eq.[36]), we can write the total energy of the system as

$$E = \sum_i K_i(R) + \sum_{i,j} W_{ij}(R) = \sum_i B_i(R) - \sum_i K_i(R). \tag{40}$$

With the dimensionless boundary radius $x_b = R/r_c$, we can rewrite the total mass as (*cf.* eq.[8])

$$M(x_b) = \sum_i M_i(R) = x_b \phi'(x_b)/\beta, \tag{41}$$

and the system energy can be calculated from Eqs. (3, 8, 10, 37, 38, 40, 41):

$$\frac{E(x_b)}{M^2(x_b)} = \frac{9}{[\phi'(x_b)]^2} \sum_i \frac{\xi_i}{\mu_i} e^{-\mu_i \phi(x_b)} - \frac{3}{2} \frac{1}{x_b \phi'(x_b)} \sum_i \frac{\chi_i(x_b)}{\mu_i}, \tag{42}$$

where

$$\chi_i(x_b) = \frac{M_i(x_b)}{M(x_b)} = \frac{\phi_i'(x_b)}{\phi'(x_b)}. \tag{43}$$

We scale the temperature relative to the stellar mass of the light particles, $T_1 = \beta_1^{-1} = kT/m_1$, which can be written as

$$\frac{T_1}{M(x_b)} = \frac{1}{\mu_1 \, x_b \, \phi'(x_b)}. \tag{44}$$

Effectively, we have here chosen to express our results in units in which $k = m_1 = 1$.

2.5.2. *Exploratory Investigations*

Previously, in §2.1 and Fig. 2, we have studied an equal-mass system under laboratory conditions: we considered our sphere to have either a fixed energy (as in a micro-canonical ensemble, with an adiabatic boundary), or to be kept at a fixed temperature (as in a macro-canonical ensemble, with a boundary which admits heat transport). In the present case, we have one extra degree of freedom, due to the presence of the second mass species, as we saw from a comparison of Fig. 1 and 4. The simplest way the visualize this extra freedom is to treat each graph in Fig. 4 separately, *i. e.* to choose fixed values for the central density contrast ξ.

Note, however, that this approach is *not* a physical laboratory equivalent of our analysis in Fig. 2, since there is no way to reach inside the sphere in order to keep the central density ratio constant upon a variation of energy or temperature. Instead, this analysis is a purely mathematical one, in order to make us more familiar with the behavior of the

two-parameter family of solutions to the isothermal two-mass system. In §2.5.3 we will come back to more realistic laboratory experiments.

In Fig. 6, we plot several energy-temperature diagrams for our two-mass system, one each for the mass ratios $\mu = 100$, 10, 5, 2. In each diagram we show the separate graphs for each of the six different choices for the central density ratio ξ which we used earlier in Fig. 4. For each choice of μ and ξ, there is a remaining choice for the dimensionless boundary radius x_b.

For $x_b \to \infty$, the central region containing the heavy stars becomes very small compared to the enclosing sphere. As a consequence, the total mass in heavy stars becomes negligible. Indeed, using the results of §2.3.4, we get $B(\infty) = -2\,E(\infty) = 0.5\,M^2$, and $T_1(\infty) = 0.5\,M$, which is the same result as we obtained in §2.1 for an equal-mass system (*cf.* Fig. 2). Indeed, at the left-hand side of all panels of Fig. 5 we see the lines spiraling in to the same limiting point.

For $x_b \to 0$, the self-gravity of the stars becomes negligible, and we reach the limit of an ideal gas. As in Fig. 2, the corresponding part of the graphs extend beyond the upper right hand side, asymptotically reaching the ideal gas relation $E = 3MT/2$. What is strikingly different, in comparison with the equal-mass case, is the much more complicated transition between a very concentrated system and the ideal gas limit. In many cases, the graphs make a detour through the positive energy area before plunging to negative energy once more, but this time at higher T_1/M, in order to complete one or more extra loops, before finally rising towards the ideal-gas limit.

This complicated behavior can be readily explained from the run of the densities, as is illustrated in Fig. 7 for the particular case $\mu = 10$ and $\xi = 10^4$. This figure is analogous to Fig. 1 for the equal-mass case, although we have chosen the positions of the letters A, B, C, and D somewhat differently, in order to make contact with Fig. 6b, where the same letters are plotted.

Let us investigate what happens when we start with a very large boundary radius, beyond the right-hand side of Fig. 7. In Fig. 6b that would correspond to the inner part of the left-most spiral. Shrinking the boundary past point D in Fig. 7 would decrease the density contrast in the light stars between center and edge, and therefore move the system up towards positive energy, past point D in Fig. 6b. Moving further past point C, the presence of the heavy stars begins to make themselves felt, as can be seen in Fig. 7 from the the fact that we are beginning to approach the radius r_e at which both densities become roughly equal.

By the time we reach point B, the heavy particles dominate in density already at the edge, and much more so in the inner parts. Therefore, the total mass in light stars has become negligible. Comparing the heavy star distribution in Fig. 7 with an equal-mass system (*cf.* Fig. 1), we see that point B is still well inside the spiral part at negative energies, and we have to go all the way to A before we escape from the spiraling area into the ideal gas limit. Indeed, this expected behavior is replicated in Fig. 6b. We now also understand why the topmost two graphs do not dip towards a second looping area: these correspond to $\xi = 0.01$ and $\xi = 1$, which excludes the possibility that the heavy stars will dominate the total mass for small values of x_b.

2.5.3. *Laboratory Experiments*

We are now in a position to switch to a more realistic, physical setting. Rather than keeping ξ constant, we keep the total mass in each species constant. In other words, we prepare our system by choosing the total number of heavy stars and the total number of light stars. After throwing these inside our sphere, we close our container, and wait till isothermal equilibrium is established (or, better, we gently inject our stars, with the required Maxwellian distribution of energies, through a narrow opening in the container). We now have no longer any control over the central density ratio ξ. The only freedom left is the variation of the total energy and/or temperature, just as in the equal mass case, since the laboratory setting is identical when we consider the container as a black box (black bottle).

The results of a number of laboratory experiments is reported in Figs. 8-11. Note that we often encounter a qualitatively similar behavior as in the equal-mass case (*cf.* Fig. 2). However, there are several differences. Sometimes the spiral part of the solution is not realized, because that part of the corresponding trajectories in Fig. 6 would have required a different total mass ratio as what was given to the system in the beginning. Note also that in many cases the total energy remains positive, for all values of the temperature (Lightman 1977). This generally happens when the total mass in the heavy component exceeds Spitzer's limit, but not by such a large extent that the light component becomes negligible. In this case a removal of the boundary sphere would have left the whole system unbound, which is another way in which the unphysical nature of such an isothermal system, violating Spitzer's bound, shows up.

3. SPITZER'S INSTABILITY

We now turn to a discussion of the mass stratification instability, derived by Spitzer (1969). Starting with a fixed background of lighter stars, Spitzer studied the effect of introducing a small fraction of heavier stars. As we have seen in the preceding section, for a sufficiently large mass ratio the equilibrium distribution of heavy stars is almost entirely confined within the core of the lighter stars. Approximating the potential of the latter as parabolic, based on their near-constant density, Spitzer showed that a small amount of heavier particles can be accommodated in the bottom of that potential well, as long as the binding energy of the heavy stars does not become too large. He gave a quantitative estimate for the limiting value of the total mass allowed in heavy stars. If the mass contained in heavier stars would exceed this value, the self-energy of these stars would prevent equilibrium to be attained. In this case, he argued, the heavier stars will continue to contract. As a consequence, the temperature of the heavy stars will continue to increase, excluding the possibility of reaching equilibrium with the cooler lighter stars.

In this section we will start with a reinterpretation of Spitzer's instability. In §3.1, instead of comparing the ratio of the total amount of mass in heavy and light stars, we will focus only on the core region of the lighter stars. We recast Spitzer's result in such a way that the outer region drops out altogether, paving the way for a replacement of the halo by a rigid boundary. In §3.2 we construct a toy model, in the form of an idealized algebraic

density distribution which allows analytic treatment, instead of the numerical solution of Poisson's equation. We show how the qualitative results of Spitzer follow directly from this model, and we indicate the region of applicability of Spitzer's original derivation. Finally, in §3.3 we give the full numerical results of our system, an isothermal two-mass model enclosed in a spherical container.

3.1. Local reformulation of Spitzer's Treatment

For a discussion of the mass stratification instability, we refer to Spitzer (1969) for the original description, or to Spitzer (1987), Ch. 3.4, for a somewhat more streamlined description, which we will follow in this section. Equations quoted below as Eq. (S3-50), etc., refer to the corresponding equations (3-50), etc., in Spitzer (1987).

The condition for the existence of an isothermal equilibrium configuration is given by Eq. (S3-55) as

$$\chi < \chi_{max} = 0.16 \tag{45}$$

where χ has been defined as

$$\chi \equiv \frac{M_2}{M_1}\left(\frac{m_2}{m_1}\right)^{3/2} = \frac{(\rho_{h1}/\rho_{h2})^{1/2}}{(1+\alpha\rho_{h1}/\rho_{h2})^{3/2}} \tag{46}$$

Here M_i and m_i are the total mass and the individual star mass in species i, respectively, with $i = 1$ for the lighter stars, and $i = 2$ for the heavier stars. The half-mass density ρ_{hi} is defined for each species as the mean density within the half-mass radius r_{hi}, the radius enclosing half the total mass in that species. The parameter α is given by Eq. (S3-52) as

$$\alpha \equiv \frac{5}{4}\frac{\rho_1(0)}{\rho_{h1}}\left(\frac{r_{m2}^2}{r_{h2}^2}\right). \tag{47}$$

Here $\rho_1(0)$ is the central density of the lighter stars, and r_{m2} is the root mean square value of the radial position r for the heavy stars. Spitzer uses a Maxwellian approximation for the velocity distribution in a parabolic approximation for the potential well, to obtain $r_{m2}/r_{h2} \simeq 1.13$. This value can be derived as $r_{m2}/r_{h2} = \sqrt{3/2}/x$, where $x \simeq 1.088$ is the solution the equation $I(x) = 1$, with $I(x)$ given by

$$I(x) = \frac{8}{\sqrt{\pi}}\int_0^x s^2 e^{-s^2}\,ds = -\frac{4}{\sqrt{\pi}}xe^{-x^2} + 2\mathrm{erf}x = 1, \tag{48}$$

which results in $r_{m2}/r_{h2} \simeq 1.126$. We have tested this value for the extreme mass ratio of $\mu = 100$. For $\xi \ll 1$, we find the same result to within 1% accuracy. For $\xi = 1$, we find a slightly larger value of 1.157. For much larger values, $\xi \gg 1$, we find values in the range $1.3 \sim 1.6$.

A number of other approximations have been made in earlier steps in Spitzer's derivation. For example, the gravitational self-binding energy W_{22} of the heavy stars was estimated by using the approximation $c \approx 0.4$ in Eq. (S1-10):

$$W_{22} = c\frac{GM_2^2}{r_{h2}} \tag{49}$$

This is indeed a good approximation within the level of accuracy of the overall discussion, as we have verified by direct numerical integration of isothermal two-mass models. We find for $\mu > 5$ that $0.40 < c < 0.50$, for all values of ξ, from $\xi \ll 1$ to $\xi \gg 1$.

By far the most serious approximation made by Spitzer stems from the uncertainty in the shape of the halo of the light stars. The parameter α depends mostly on the choice of density contrast $\rho(0)/\rho(r_h)$ between center and half-mass radius of the star cluster. For a Plummer model, which has a lower density contrast than most globular clusters, $\alpha = 7$. If we take a more strongly concentrated model with $\rho(0)/\rho(r_h) \simeq 100 - 1000$, corresponding to some of the more concentrated clusters observed, we would have $\alpha \simeq 160 - 1600$.

This is clearly the most drastic of the different approximations made. However, even the uncertainty of nearly three orders of magnitude in α does not affect the physical significance of Spitzer's treatment, as we now demonstrate by reinterpretation in terms of core parameters only.

Substituting $r_{m2}/r_{h2} = 1.126$ in Eq. (47), we can write

$$\alpha\rho_{h1} = 1.585\rho_1(0). \tag{50}$$

If we substitute this in Eq. (46), we can introduce a local substitute for χ in the form of χ_c, with

$$\chi_c \equiv \frac{M_2}{M_{c1}}\left(\frac{m_2}{m_1}\right)^{3/2} = \left(\frac{M_1}{M_{c1}}\right)\left(\frac{\rho_{h1}}{\rho_1(0)}\right)^{1/2}\left(\frac{\rho_1(0)}{\rho_{h2}}\right)^{1/2}\left(1 + 1.585\frac{\rho_1(0)}{\rho_{h2}}\right)^{-3/2}, \tag{51}$$

where M_{c1} is defined in Eq. (34) as the core mass for the isothermal distribution of the light stars in the limit in which the heavy stars can be neglected.

Note that the first two factors in Eq. (51) scale in such a way that the dependence on central concentration nearly drops out. To illustrate this, we can even take the limit of an infinite isothermal sphere for the mass distribution of the light particles. In this case, we can use the results of §2.3.4, together with Eqs. (8) and (34), to obtain

$$\left(\frac{M_1}{M_{c1}}\right)\left(\frac{\rho_{h1}}{\rho_1(0)}\right)^{1/2} = 2.11 \tag{52}$$

This leads us to an alternative formulation of the mass stratification instability. Instead of limiting the ratio of total masses, Eq. (46), we limit the total mass in heavy stars, expressed as a fraction of the core mass of the light stars:

$$\chi_c \equiv \frac{M_2}{M_{c1}}\left(\frac{m_2}{m_1}\right)^{3/2} = 2.1\left(\frac{\rho_1(0)}{\rho_{h2}}\right)^{1/2}\left(1 + 1.6\frac{\rho_1(0)}{\rho_{h2}}\right)^{-3/2}. \tag{53}$$

Here we have chosen to use the constant derived in Eq. (52), which is the natural limit for an advanced state of core collapse. If we would be more interested in a less concentrated star cluster, we could take the example of a Plummer model, for which the constant at the right hand side of Eq. (52) is 2.46.

The physical interpretation is as follows. Since the heavy stars couple dynamically only with those light stars which are well withing the core, the stability criterion should be independent of the mass distribution of the light stars in the halo. Thus, the only natural scale to compare the upper limit for the total mass in heavy stars is the core mass of the light stars. As a consequence, a shrinking of the core reduces the total mass of the heavy stars in proportion to the decrease of the core mass.

3.2. Toy Model in Enclosing Container

We are now in a position to compare Spitzer's (1987) derivation directly with our models. But before doing so, we first simplify our models in order to highlight the basic physical structure. The resulting family of toy models is defined by the density profiles plotted in Fig. 12a. For the lighter stars, the core density is taken to be constant up to the core radius r_{c1}, with a drop-off $\propto r^{-2}$ outside the core. For the heavier stars a similar approximation has been applied, with the extra feature that a drop-off steeper than $\propto r^{-2}$ has been approximated by a cut-off.

Specifically, we have:

$$\rho_1(r) = \begin{cases} \rho_1(0), & \text{for } r \leq r_{c1}; \\ \rho_1(0)\,(r/r_{c1})^{-2}, & \text{for } r \geq r_{c1}. \end{cases} \tag{54}$$

and

$$\rho_2(r) = \begin{cases} \xi\,\rho_1(0), & \text{for } r \leq r_{c2}; \\ \xi\,\rho_1(0)\,(r/r_{c2})^{-2}, & \text{for } r_{c2} \leq r \leq r_e; \\ 0, & \text{for } r \geq r_e. \end{cases} \tag{55}$$

There are two qualitatively different configuration. Either the heavy stars dominate in mass density in the center (dash-dotted line), which implies $\xi \geq 1$, in which case the cutoff occurs around the point where both densities become comparable, or the light stars dominate already in the center (dashed line), in which case the heavy stars are given a constant density distribution until they reach the cut-off. In the latter case, there are only two regimes described by Eq. (t2): with $r_{c2} = r_e$ the intermediate regime is not present.

What are the relations between the three parameters r_{c1}, r_{c2} and r_e? In the accurate models presented in §2.3, we found $r_{c1} = (\xi\mu)^{1/2} r_{c2}$ and $r_e = \xi^{1/2} r_{c2}$. In our approximate model defined by Eq. (t1, t2), we expect these relations to hold approximately. However, since Eq. (t1, t2) are not exact, we have some freedom in our definitions of the relations between r_{c1}, r_{c2} and r_e. Rather than repeating the definitions of §3.2 exactly, we can use this freedom to guarantee that our toy model obeys the virial theorem exactly. The resulting calculations are somewhat lengthy, and are therefore presented in Appendix B.

Our toy model is a reasonable approximation for models with $\mu \gg 1$, which can be verified directly by a comparison of Figs. 4a and 12a. Let us now compare the behavior of our toy model, enclosed in a spherical container, with that of Spitzer's treatment of a free cluster. We keep the radius R of the container and the temperature T constant, as well as the total mass M_1 and the central density $\rho_1(0)$ of the light stars. As an adjustable parameter, we only vary the central density ratio $\rho_2(0)/\rho_1(0)$. Fig. 12c shows the resulting

total mass M_2 in heavy stars, expressed in the units used by Spitzer, for the specific choice $\mu \equiv m_2/m_1 = 100$ and $T_1 \equiv kT/m_1 = 0.45M$.

For low central densities in heavy stars, $\rho_2(0) \lesssim \rho_1(0)$, we have $M_2/M_1 \propto \rho_2(0)/\rho_1(0)$. This increase flattens off soon after the heavy stars begin to dominate the central density, reaching the maximum value $M_2/M_1 = 1.88 \times 10^{-4}$ for $\rho_2(0)/\rho_1(0) = 5.59$, where $\rho_{h2}/\rho_{h1} = 20.8$. Thereafter, M_2 declines slightly, by about 10%. This qualitative behavior is in accord with Fig. 12a: in the limit $\rho_2(0)/\rho_1(0) \to \infty$, the descending part of the dash-dotted line, where most of the mass in heavy stars resides, remains nearly constant, since the cut-off radius r_e is only weakly dependent on the central density (see Appendix B). A similar behavior is clearly visible in Fig. 4a.

When we plot the total mass ratio as a function of the ratio of half-mass densities ρ_{h2}/ρ_{h1}, we obtain Fig. 12b. The variation is entirely due to that of ρ_{h2}, since the density distribution of the light stars is fixed in our toy model. We see that even for $\rho_2(0)/\rho_1(0) \to \infty$, the density ratio reaches a finite value $\rho_{h2}/\rho_{h1} \to 35.9$. This is again a consequence of the fact that the bulk of the mass distribution of the heavy stars in Fig. 12a is not affected in taking this limit.

We are now in a position to make a direct comparison with Spitzer's approximate analytic derivation. In Fig. 12d we have plotted Eq. (46), corresponding to Eq. (3-54) of Spitzer (1987). As we discussed above, the parameter α is highly model-dependent. Spitzer's preferred choice is $\alpha = 5.6$, in the middle of the range for polytropes with polytropic index n between 3 and 5. We have plotted three curves to bracket his choice, for α values of 4, 6, and 8, all corresponding to cluster models with relatively little central concentration.

It is clear that Fig. 12d gives a very reasonable qualitative agreement with Fig. 12b, especially for the value $\alpha = 4$. However, the extreme right hand sides of the curves in Fig. 12d are unphysical, and cannot correspond to equilibrium states attainable for our toy model, no matter how high the central density in the heavy stars. This does not effect the validity of Spitzer's derivation, since the curves are not affected around the position of the maximum value of the mass ratio.

3.3. Real Models in Enclosing Container

Returning to our numerical solutions of the exact equations for isothermal equilibrium, we can repeat the analysis of the previous section. The results are given in Fig. 13 for $T_1 = 0.45\,M$. The results are plotted for the solutions of the lower energy branch shown in Fig. 6, thus, the system contains mostly the light component, and is self-bounded ($E < 0$). In the first panel, apart from the damped wave shape at the right hand side, the run of the total mass ratios is very similar to the corresponding panel in the case of our toy model, Fig. 12d. Fig. 13b shows how our alternative treatment of the Spitzer instability, in terms of the core mass rather than total mass in light stars (§3.1), indeed gives very similar results. The behavior at the limit $\xi \to \infty$ confirms our analytic estimate in Eq. (35). Fig. 13c shows how insensitive the half-mass density in light particles is. Even an increase in central density ratio of eight orders of magnitude leads to a decrease in $\rho_{h1}/\rho_1(0)$ of

only 15%. This provides justification for the approximation made in our toy model, where this ratio was artificially held constant.

The comparison with Spitzer's analysis is finally given in Fig. 13d. A comparison with Figs. 12a,c shows that the toy model has indeed captured the basic physics, and that the downward sloping lines at the right-hand side of Fig. 12d cannot be reached. The spiraling behavior of Fig. 13d is related to the slightly wavy character of the correct drop-off in density, visible in the right-hand side of Fig. 4a, and related to the fact that Poisson's equation is a second-order differential equation (Chandrasekar 1939 gives an analytic approximation for this behavior in the limit of large radii).

The last two panels of Fig. 13 reinforce our conclusions. Fig. 13e shows again how the approximation of a fixed light star density profile is quite accurate, with only a small change in light star core radius expressed as a function of the fixed radius R of the enclosing boundary. Fig. 13f is given here in conjunction with Fig. 13c in order to provide complete information, enabling the reader to complete the translation from Fig. 13a to Fig. 13d step by step.

For comparison, a similar analysis for less extreme mass ratios leads to Figs. 14-16. Notice that already in Fig. 14b, the flattening off of the M_2 in units of the light star core mass M_1 is lost. The reason can be gleaned from Fig. 4b. Rather than reaching a limiting density profile for $\rho_2(0)/\rho_1(0) \to \infty$, the density ratios at any fixed point inside the core of the light stars keep creeping up noticeably. This is caused by the break-down of the constant-density approximation for the density in the light stars. While the heavy stars are virtually all confined to the core of the light stars for $\mu = 100$, this is no longer strictly the case for $\mu = 10$, and even less so for lower μ values, as can be seen from Figs. 4c,d. Consequently, the total mass ratios keep growing in Figs. 14b, and even more so in Fig. 15b. Fig. 16b also tends to a steep growth at first, but then stops abruptly, because no equilibrium solutions are present for $\mu = 2$ with the required $T_1/M = 0.45$ for ξ values larger than about 1/3. This follows from Fig. (6d).

Another indication that the toy model approximations, valid for high μ values, break down for $\mu \lesssim 10$ can be seen in Figs. 14c and 15c, where the half-mass density in light stars begins to drop sharply with respect to the light star central density. Fig. 16c shows the opposite behavior. The reason here is that the potential of the heavy component is no longer a small perturbation at $T_1/M = 0.45$, as can be seen in Fig. 4d, where the notion of a core radius for the light stars loses its meaning for $\xi \gg 1$.

The reason that all lines in Fig. 16 are truncated follows from the behavior of the lines in Fig. 6d. There we see that for relatively low values of T_1/M, such as our case in which $\log(T_1/M) = -0.347$, only relatively low values of ξ can be realized; higher ξ curves all are located in the higher temperature region of Fig. 16d. To give at least some impression of the complexity of discussing laboratory experiments, we have added Fig. 17 to show the effect of slightly raising the temperature, to $T_1/M = 0.49$, corresponding to $\log(T_1/M) = -0.310$.

In this last case, an interesting new phenomenon occurs: there is a gap for $1.6 < \xi < 3.4$ which can be traced back to the counterintuitive behavior of the lines in Fig. 6d. In that figure, we have added the line $\xi = 2.5$ to illustrate how our temperature choice in Fig. 17 avoids this line. Thus, what makes the gap possible is the fact that the line for

$\xi = 2.5$ does not lie neatly in between the lines for $\xi = 1$ and $\xi = 100$. Ultimately, this in turn is a consequence of the fact that for ξ values of order unity we cannot analyze the system qualitatively as being centrally dominated by one of the two mass groups.

Finally, comparing Spitzer's analysis with our models for lower μ values, we find from Figs. 14d and 15d that the total mass ratios behave in a way qualitatively similar as for higher μ values, the break-down of our toy model approximations notwithstanding, as long as we choose a temperature value T_1/M such that we allow high density contrast models to form.

4. CONCLUSIONS

Multi-mass systems are notoriously difficult to treat analytically, even in approximation. The discovery by Spitzer (1969) of the mass stratification instability was a remarkably creative *tour de force*. It has provided a central guideline for our understanding of the evolution of realistic, multi-mass star clusters. In its qualitative features, this instability has been observed in a variety of large-scale simulations of star clusters. However, mass segregation always competes with the overall dynamical evolution of the star system as a whole, since both processes occur on time scales comparable to the two-body relaxation time. As a result, it has been difficult to investigate the instability in a quantitative fashion.

We have presented an alternative form of a quantitative investigation of the mass stratification instability. We have enclosed our star cluster within a spherical adiabatic wall, thereby giving the cluster the opportunity to reach exact isothermal equilibrium. The set of all possible equilibrium solutions, apart from scaling in mass, length, and time, forms a two-parameter family (for a fixed ratio of stellar masses). If we consider our cluster-in-a-bottle as a piece of laboratory apparatus, it is natural to fix the total mass in each of the two species of stars. With this constraint, we are left with a one-parameter family of equilibria. This enabled us to plot relations between the various thermodynamic quantities describing the system, such as the temperature and the energy. The results are given in §2, and plotted in Fig. 6.

We then investigated in detail in §3 the various assumptions made by Spitzer in his derivation of the mass stratification instability. We started by recasting Spitzer's analysis into a local form, by using only quantities defined inside the core of the light stars. This enabled us to bypass the largest uncertainty, caused by the freedom in choosing the shape of the halo of the light stars. We then introduced an toy model, containing the essential features of a two-mass model but with a highly simplified set of density distributions.

Within the context of our toy model, we showed how Spitzer's analysis of a maximum mass in heavy stars can be interpreted as a one-dimensional series of isothermal equilibrium solutions. This series is physically attainable up to, but not substantially past, the point were the maximum amount of heavy stars is realized. This behavior is shown in Fig. 12b. Spitzer's original derivation is plotted in Fig. 12d. In both cases, low values of ρ_{h2}, the density of the heavy stars as averaged over the region enclosed by the half-mass radius r_{h2}, correspond to small values of M_2, for a (nearly) fixed distribution of light stars. Increasing ρ_{h2} first leads to higher M_2, until a maximum is reached.

The physical reason for the existence of a maximum mass M_2, as explained by Spitzer, is that the self-binding energy of the heavy stars has become comparable to the interaction energy between the heavy and light stars. The simplest interpretation of Fig. 12d would suggest that for much higher values of ρ_{h2}, the downturn of the graphs at the right-hand side would de dictated by the need to avoid raising the velocity dispersion of the heavy stars, something which can only be achieved by lowering M_2 for increasing ρ_{h2}. However, this interpretation is not correct, simply because the right hand part of Fig. 12d cannot be physically realized. Fig. 12c shows how M_2 remains nearly constant when the central density is raised. The explanation for this difference in behavior is that the half-mass density ρ_{h2} reaches a finite limit when the central density $\rho_2(0) \to \infty$.

The same qualitative behavior is shown for the numerical solutions of the fully self-consistent isothermal two-mass models, given in Figs. 13-16. Note from the first panel of each figure that their is little variation in the maximum values of $\mu^{3/2} M_2/M_1$ as a function of μ, confirming the accuracy of Spitzer's procedure. A comparison with the second panel in each of these figures shows that our local analysis in terms of core quantities is only valid for very large mass ratios (Fig. 13b), and becomes increasingly less useful for smaller ratios. This follows from the increase in break-down of the approximation of constancy for the central density of the light stars (*cf.* Fig. 4).

The behavior for small mass ratios, such as $\mu = 2$, is more complex, since there are ranges in ξ which cannot be reached for fixed T_1/M. This explains the truncations in Fig. 16, and the gaps in Fig. 17. The appearance of these restrictions are discussed at the end of §3.3.

Summing up, we have presented a number of detailed terrain maps of the complex landscape of isothermal two-mass systems, enclosed in a fixed container. Although our two-mass system is still much simpler in structure than the general multi-mass or continuous-mass-distribution systems, its behavior is complex enough to shed light on a number of issues which do not show up in the simpler equal-mass case. Therefore, these maps will provide useful assistance in the interpretation of the detailed output of present and future simulations of star clusters containing a stellar mass spectrum.

We thank Lyman Spitzer for his comments on the manuscript.

REFERENCES

Aguilar, L., Hut, P., & Ostriker, J.P. 1988, ApJ, 335, 720

Antonov, V.A. 1962, Vestnik Leningrad Univ., 7, 135; English translation in Dynamics of Star Clusters, I.A.U. Symp. 113 (1985), eds. J. Goodman & P. Hut (Reidel, Dordrecht), p. 525

Binney, J.J. and Tremaine, S.D. 1987, Galactic Dynamics [Princeton Univ. Press]

Chandrasekhar, S. 1939, An Introduction to the Study of Stellar Structure (Univ. of Chicago Pr.; reprinted 1958 by Dover Pr.)

Chernoff, D.F. & Weinberg, M.D., 1990, ApJ, 351, 121

Cohn, H. 1980, ApJ, 242, 765

Dejonghe, H. 1984, AaA, 133, 225

Elson, R., Hut, P. & Inagaki, S. 1987, ARAA, 25, 565

Hénon, M. 1960, Ann. d'Astrophys., 23, 668

Hernquist, L. 1990, ApJ, 356, 359

Hut, P. 1991, in X-ray Binaries and The Formation of Binary and Millisecond Pulsars, ed. E.P.J. van de Heuvel & S. Rappaport

Inagaki, S. 1980, PASJ, 32, 213

Ipser, J.R. & Kandrup, H.E. 1980, ApJ, 241, 1141

Jaffe, W. 1983, MNRAS, 202, 995

Katz, J. & Taff, L.G. 1983, ApJ, 264, 476

King, I. 1989 in Dynamics of Dense Stellar Systems, ed. D. Merritt [Cambridge Univ. Pr.], p. 157.

Lightman, A. 1977, ApJ, 215, 914

Lynden-Bell, D. &Wood, R. 1968, MNRAS, 138, 495

Makino, J. & Hut, P. 1991, ApJ. 383, 181

Merritt, D. 1981, AJ, 86, 318

Pryor, C., McClure, R.D., Fletcher, J.M. & Hesser, J.E. 1989, AJ, 98, 596

Saito, M. & Yoshizawa, M. 1976, AaSS, 41, 63

Spitzer, L. 1969, ApJ, 158, L139

Spitzer, L. 1987, Dynamical Evolution of Globular Clusters (Princeton: Princeton University Press)

Taff, L.G., van Horn, H.M., Hansen, C.J. & Ross, R.R. 1975, ApJ 197, 651

Yoshizawa, M., Inagaki, S., Nishida, M.T., Kato, S., Tanaka, Y., and Watanabe, Y. 1978, PASJ, 30, 279

Appendix A: The Equal-Mass Toy Model

We consider the following extremely simple approximation for the density distribution in an equal-mass isothermal system:

$$\rho(r) = \begin{cases} \rho(0) & \text{for} \quad r \le r_c; \\ \rho(0)\left(\dfrac{r}{r_c}\right)^{-2} & \text{for} \quad r \ge r_c. \end{cases} \tag{A1}$$

The mass enclosed within radius r is

$$M(r) = 4\pi \int_0^r \tilde{r}^2 d\tilde{r}\, \rho(\tilde{r}) = \begin{cases} M_c\, y^3 & \text{for} \quad y \le 1; \\ 3M_c\left(y - \dfrac{2}{3}\right) & \text{for} \quad y > 1, \end{cases} \tag{A2}$$

where we have introduced $y = r/r_c$ as a dimensionless radius, and

$$M_c = \frac{4\pi}{3}\rho(0)\, r_c^3, \tag{A3}$$

as the core mass. Assuming that the system is enclosed by a spherical boundary of radius R, with $R > r_c$, we can write the total mass of the system as

$$M = (3y_b - 2)M_c, \tag{A4}$$

where $y_b = R/r_c$ is the dimensionless radius of the boundary. Using Eqs. (A1), (A2) and (A3), we can calculate the potential energy of the system to be

$$\begin{aligned} W &= -4\pi G \int_0^R r\, dr\, \rho(r)\, M(r) \\ &= -\frac{3y_b}{5\,(3y_b - 2)^2}(15\, y_b - 10 \ln y_b - 14)\frac{GM^2}{R}. \end{aligned} \tag{A5}$$

The kinetic energy of the system is defined as (Eq.[38])

$$K = \frac{3M}{2\beta}, \tag{A6}$$

where $\beta = m/kT$, and T the temperature of the system. According to the virial theorem (Eq.[36]), the potential energy is related to the kinetic energy by

$$W = B - 2\,K, \tag{A7}$$

where the boundary term B is proportional to the pressure P at the boundary (Eq.[37]):

$$B = 4\pi R^3 P(R) = 4\pi R^3 \frac{\rho(R)}{\beta} = \frac{3y_b}{3y_b - 2}\frac{M}{\beta}. \tag{A8}$$

Thus, Eq. (A7) can be written as

$$W = -\frac{6\,(y_b - 1)}{3y_b - 2}\frac{M}{\beta}. \tag{A9}$$

Comparing Eq. (A5) with (A9), we obtain

$$\frac{R}{GM\beta} = \frac{y_b}{10\,(y_b - 1)(3y_b - 2)}(15\,y_b - 10\ln y_b - 14). \tag{A10}$$

The total energy of the system is then

$$E = K + W = B - K = -\frac{3\,(y_b - 2)}{2\,(3y_b - 2)}\frac{M}{\beta}. \tag{A11}$$

Or using Eq. (A10), we can write

$$\frac{ER}{GM^2} = -\frac{3\,y_b\,(y_b - 2)}{20\,(y_b - 1)(3y_b - 2)^2}(15\,y_b - 10\ln y_b - 14). \tag{A12}$$

The temperature-energy diagram, defined by Eqs. (A10) and (A12), is plotted in Fig. 3. In the limit of a very large density contrast between the center and the edge of our enclosed system, we have $y_b \to \infty$, and we find that our system to approach the limiting values $R/(GM\beta) = 1/2$ and $ER/(GM^2) = -1/4$.

Appendix B: The two-mass toy model

We now extend the model of Appendix A to a system containing stars with two different stellar masses, m_1 and m_2, with $m_1 < m_2$. As before, the density distribution of the light stars is given by

$$\rho_1(r) = \begin{cases} \rho_1(0) & \text{for} \quad r \leq r_{c1}; \\ \rho_1(0)\left(\dfrac{r}{r_{c1}}\right)^{-2} & \text{for} \quad r \geq r_{c1}. \end{cases} \tag{B1}$$

For the density of the heavy stars, there are two qualitatively different configurations. In the first case the heavy stars dominate in mass density in the center, we approximate their density distribution as

$$\rho_2(r) = \begin{cases} \xi\,\rho_1(0) & \text{for} \quad r \leq r_{c2}; \\ \xi\,\rho_1(0)\left(\dfrac{r}{r_{c2}}\right)^{-2} & \text{for} \quad r_{c2} \leq r \leq r_e; \\ 0 & \text{for} \quad r \geq r_e, \end{cases} \tag{B2a}$$

where the density ratio ξ at the center is greater than the density $\xi_e \sim 1$ at the cutoff radius r_e at which point the densities of the two types of stars become comparable. At this point we still have some freedom in the exact choice for the parameter r_e, which determines the value ξ_e. Rather than giving a somewhat arbitrary definition here, we can use this freedom to guarantee that the virial theorem will be satisfied exactly. This will introduce a dependency of r_e and ξ_e on the the mass ratios μ and the boundary radius R, as we will show explicitly below, following Eq. (B15).

In the second case the light stars dominate already in the center (in a sense which will be made quantitatively precise below, see Eq. B23 for a specific example). Here we approximate the density distribution of the heavy stars as being constant until reaching the cut-off:

$$\rho_2(r) = \begin{cases} \xi\,\rho_1(0) & \text{for} \quad r \leq r_e; \\ 0 & \text{for} \quad r \geq r_e, \end{cases} \tag{B2b}$$

The core radius r_{c2} of the heavy stars is related to that of the light stars r_{c1} by Eq. (17), *i.e.*,

$$r_{c1} = \sqrt{\mu\xi}\, r_{c2}. \tag{B3}$$

By integrating Eq. (B1), we obtain the mass of the light stars enclosed within radius r:

$$M_1(r) = \begin{cases} M_{c1}\, y^3 & \text{for} \quad y \leq 1; \\ 3M_{c1}\left(y - \dfrac{2}{3}\right) & \text{for} \quad y \geq 1, \end{cases} \tag{B4}$$

where $y = r/r_{c1}$ is the dimensionless radius, and

$$M_{c1} = \frac{4\pi}{3}\rho_1(0)\, r_{c1}^3, \tag{B5}$$

is the core mass of the light stars. Similarly, the mass of the heavy stars enclosed within radius r is

$$M_2(r) = \begin{cases} \xi\, M_{c1}\, y^3 & \text{for} \quad y \le \dfrac{1}{\sqrt{\mu\xi}}; \\ \dfrac{3}{\mu} M_{c1}\left(y - \dfrac{2}{3\sqrt{\mu\xi}}\right) & \text{for} \quad \dfrac{1}{\sqrt{\mu\xi}} \le y \le y_e; \\ \dfrac{3}{\mu} M_{c1}\left(y_e - \dfrac{2}{3\sqrt{\mu\xi}}\right) & \text{for} \quad y \ge y_e, \end{cases} \tag{B6}$$

where $y_e = r_e/r_{c1}$ is the dimensionless cutoff radius, and we have assumed that $\xi \ge \xi_e$. Assuming further that

$$R > r_{c1} > r_e > r_{c2}, \tag{B7}$$

we can write the total mass of the light stars as

$$M_1 = (3y_b - 2)M_{c1}, \tag{B8}$$

where $y_b = R/r_{c1}$ is the dimensionless radius of the boundary. For the heavy stars, we have

$$M_2 = \begin{cases} \xi\, M_{c1}\, y_e^3 & \text{for} \quad \xi \le \xi_e; \\ \dfrac{3}{\mu} M_{c1}\left(y_e - \dfrac{2}{3\sqrt{\mu\xi}}\right) & \text{for} \quad \xi \ge \xi_e. \end{cases} \tag{B9}$$

By using Eqs. (39) and (B1-6), we can calculate the relevant potential energy terms needed in the various forms of the virial theorem, as discussed in Appendix C:

$$\begin{aligned} W_{21} &= -\frac{3GM_{c1}^2 y_b}{R}\left[-\frac{2}{15}\mu^{-5/2}\xi^{-3/2} + \frac{1}{3}\mu^{-1}y_e^3\right]; \\ W_{22} &= -\frac{3GM_{c1}^2 y_b}{R}\left[-\frac{14}{5}\mu^{-5/2}\xi^{-1/2} + 3\mu^{-2}y_e - 2\mu^{-5/2}\xi^{-1/2}\ln(\sqrt{\mu\xi}\, y_e)\right]; \\ W_{11} &= -\frac{3GM_{c1}^2 y_b}{R}\left[-\frac{14}{5} + 3y_b - 2\ln y_b\right]; \\ W_{12} &= -\frac{3GM_{c1}^2 y_b}{R}\left[-\frac{1}{5}\mu^{-5/2}\xi^{-3/2} - \frac{1}{2}\mu^{-1}y_e^3 + \frac{3}{2}\mu^{-1}y_e - \mu^{-3/2}\xi^{-1/2}\right. \\ &\qquad \left. +(3\mu^{-1}y_e - 2\mu^{-3/2}\xi^{-1/2})\ln y_b\right], \end{aligned} \tag{B10}$$

for $\xi > \xi_e$, and

$$
\begin{aligned}
W_{21} &= -\frac{3GM_{c1}^2 \xi y_b}{R}\frac{y_e^5}{5}; \\
W_{22} &= -\frac{3GM_{c1}^2 \xi^2 y_b}{R}\frac{y_e^5}{5}; \\
W_{11} &= -\frac{3GM_{c1}^2 y_b}{R}\left[-\frac{14}{5} + 3y_b - 2\ln y_b\right]; \\
W_{12} &= -\frac{3GM_{c1}^2 \xi y_b y_e^3}{R}\left[-\frac{4}{5}y_e^2 + 1 + \ln y_b\right],
\end{aligned}
\tag{B11}
$$

for $\xi \leq \xi_e$.

We are now in a position to write the virial theorem (Eq.[36]) by using Eqs. (B8-11). First, let us consider the case $\xi \geq \xi_e$. Since there is no boundary term for the heavy stars, the virial theorem for the heavy stars reads

$$
\begin{aligned}
\frac{kTR}{GMm_1} &= \frac{R\mu}{3GMM_2}(-W_{21} - W_{22}) \\
&= \frac{y_b}{(3y_b - 2 + 3\mu^{-1}y_e - 2\mu^{-3/2}\xi^{-1/2})(3\mu^{-1}y_e - 2\mu^{-3/2}\xi^{-1/2})}\left[-\frac{2}{15}\mu^{-3/2}\xi^{-3/2} + \frac{1}{3}y_e^3\right. \\
&\left. -\frac{14}{5}\mu^{-3/2}\xi^{-1/2} + 3\mu^{-1}y_e - 2\mu^{-3/2}\xi^{-1/2}\ln(\sqrt{\mu\xi}\, y_e)\right].
\end{aligned}
\tag{B12}
$$

The boundary term B_1 for the light mass is

$$
B_1 = 4\pi R^3 P(R) = 4\pi R^3 \frac{\rho_1(R)}{\beta_1} = 3y_b M_{c1}\frac{kT}{m_1}. \tag{B13}
$$

Thus the virial theorem for the light stars can be written as

$$
\begin{aligned}
\frac{kTR}{GMm_1} &= \frac{R}{3GM(M_1 - y_b M_{c1})}(-W_{11} - W_{12}) \\
&= \frac{y_b}{(3y_b - 2 + 3\mu^{-1}y_e - 2\mu^{-3/2}\xi^{-1/2})(2y_b - 2)}\left[-\frac{14}{5} + 3y_b - 2\ln y_b - \frac{1}{5}\mu^{-5/2}\xi^{-3/2}\right. \\
&\left. -\frac{1}{2}\mu^{-1}y_e^3 + \frac{3}{2}\mu^{-1}y_e - \mu^{-3/2}\xi^{-1/2} + (3\mu^{-1}y_e - 2\mu^{-3/2}\xi^{-1/2})\ln y_b\right].
\end{aligned}
\tag{B14}
$$

Equating Eq. (B12) with (B14), we obtain

$$
\begin{aligned}
&(2y_b - 2)\left[-\frac{2}{15}\mu^{-3/2}\xi^{-3/2} + \frac{1}{3}y_e^3 - \frac{14}{5}\mu^{-3/2}\xi^{-1/2} + 3\mu^{-1}y_e - 2\mu^{-3/2}\xi^{-1/2}\ln(\sqrt{\mu\xi}\, y_e)\right] \\
&= (3\mu^{-1}y_e - 2\mu^{-3/2}\xi^{-1/2})\left[-\frac{14}{5} + 3y_b - 2\ln y_b - \frac{1}{5}\mu^{-5/2}\xi^{-3/2} - \frac{1}{2}\mu^{-1}y_e^3\right. \\
&\left. + \frac{3}{2}\mu^{-1}y_e - \mu^{-3/2}\xi^{-1/2} + (3\mu^{-1}y_e - 2\mu^{-3/2}\xi^{-1/2})\ln y_b\right].
\end{aligned}
\tag{B15}
$$

When $y_b \gg 1$ and $\xi \gg 1$, Eq. (B14) gives $kTR/(GMm_1) = 1/2$. From Eqs. (B15) and (B2), we find $y_e = 3/\sqrt{2\mu}$, and $\rho_2(r_e) = \frac{2}{9}\rho_1(0)$. These turn out to be exactly identical to the results we found in § 2.3.2.

In the second case, with $\xi \leq \xi_e$, we can write the virial theorem for both components as

$$\frac{kTR}{GMm_1} = \frac{\mu\, y_b\, y_e^2\,(1+\xi)}{5(3y_b - 2 + \xi y_e^3)}, \tag{B16}$$

and

$$\frac{kTR}{GMm_1} = \frac{y_b}{(3y_b - 2 + \xi y_e^3)(2y_b - 2)}\left[-\frac{14}{5} + 3y_b - 2\ln y_b + \xi y_e^3\left(-\frac{4}{5}y_e^2 + 1 + \ln y_b\right)\right]. \tag{B17}$$

Equating Eq. (B16) with (B17), we get

$$(2y_b - 2)\,\mu\, y_e^2(1+\xi) = 5\left[-\frac{14}{5} + 3y_b - 2\ln y_b + \xi y_e^3\left(-\frac{4}{5}y_e^2 + 1 + \ln y_b\right)\right]. \tag{B18}$$

We are now in a position to determine the value of ξ_e. We can do this by starting with the special intermediate case in which $\xi = \xi_e$, in which both Eqs. (B15) and (B18) should be both satisfied. For each pair of values for μ and y_b, we can then solve for both ξ_e and y_e directly from Eqs. (B15) and (B18).

We will illustrate this procedure with the specific example of $\mu = 100$ and $kTR/(GMm_1) =$ 0.45. In this case, $y_b \gg 1$, and $y_e \sim 1/\sqrt{\mu} \ll 1$. Since $\xi_e \sim 1$, Eq. (B14) becomes

$$0.45 \simeq \frac{y_b}{(3y_b - 2)(2y_b - 2)}\left(-\frac{14}{5} + 3y_b - 2\ln y_b\right), \tag{B19}$$

which has a solution for the boundary radius of $y_b \simeq 10.6$. For convenience, we define a new parameter $z = \sqrt{\mu}\, y_e$, which is of order of unity. Eq. (B9) can then be written as

$$\mu^{3/2}\, M_2 = \begin{cases} \xi\, M_{c1}\, z^3 & \text{for} \quad \xi \leq \xi_e; \\ 3M_{c1}\left(z - \dfrac{2}{3\sqrt{\xi}}\right) & \text{for} \quad \xi \geq \xi_e. \end{cases} \tag{B20}$$

Combining Eqs. (B15) and (B18), we get the approximate result

$$6.40\, z^3 - 15.2\, z = \xi^{-1/2}[38.4\, \ln(\sqrt{\xi}\, z) + 5.20 + 2.56\, \xi^{-1}], \tag{B21}$$

for $\xi > \xi_e$, and

$$z = \sqrt{\frac{6.32}{1+\xi}}, \tag{B22}$$

for $\xi \leq \xi_e$. By combining Eq. (B21) and Eq. (B22) we get the cut-off value

$$\xi_e = 0.185, \tag{B23}$$

and $z = 2.31$ at $\xi = \xi_e$. In general, given a central density ratio ξ, we can calculate the cutoff radius z from Eqs. (B21) and (B22). The radius z decreases monotonically with increasing ξ, but is restricted to lie within the interval $2.51 > z > 1.55$ for $0 < \xi < \infty$. From Eqs. (B8) and (B20), we can derive the half-mass mean densities, as

$$\frac{\rho_{h1}}{\rho_1(0)} = 108\,\frac{3x_b - 2}{(3x_b + 2)^3}, \tag{B24}$$

and

$$\frac{\rho_{h2}}{\rho_1(0)} = \begin{cases} \xi, & \text{for} \quad \xi \le \dfrac{16}{9z^2}; \\ \dfrac{108\,\xi(3\sqrt{\xi}\,z - 2)}{(3\sqrt{\xi}\,z + 2)^3}, & \text{for} \quad \xi \ge \dfrac{16}{9z^2}. \end{cases} \tag{B25}$$

The results from Eqs. (B8), and (B20-25) are plotted in Fig. 12b and 12c. Substituting $y_b = 10.6$ into Eqs. (B8) and (B24), we get $M_1 = 29.8\,M_{c1}$, and $\rho_{h1} = 0.083\,\rho_1(0)$. M_2/M_1 reaches the maximum value $M_2/M_1 = 0.186\,\mu^{-3/2}$ for $\rho_2(0)/\rho_1(0) = 9.77$, where $\rho_{h2}/\rho_{h1} = 22.6$. When $\xi \gg 1$, from Eqs. (B21), (B20), and (B25), we get $z = 1.55$, $M_2 = 4.63\,\mu^{-3/2}\,M_{c1} = 0.156\,\mu^{-3/2}\,M_1$, and $\rho_{h2} = 4.99\,\rho_1(0) = 60.0\,\rho_{h1}$. All these values are remarkably close to the results for the real isothermal models with $\mu = 100$ and $kTR/(GMm_1) = 0.45$ (Fig. 13).

Appendix C: The virial theorem applied to individual species.

The virial theorem tells us how large the average velocity has to be for each species, in order to maintain equilibrium, i.e. to avoid imploding or exploding. This balance, on average, of centripetal and centrifugal forces (gravity and inertia) takes the simplest form in the circular Kepler orbit, where the gravitational force obeys:

$$F = \frac{v^2}{r} \tag{C1}$$

For an elliptic orbit, $v = v(t)$ and $r = r(t)$, but here too we can check explicitly that:

$$\langle v^2 \rangle = \langle F r \rangle \tag{C2}$$

Let us consider a spherical star cluster, of mass M, containing stars of a finite number of species, each having a total mass M_i and an individual stellar mass m_i. For such a system, the above equation generalizes to

$$M_i \langle v_i^2 \rangle = \int \langle F\ r_i \rangle dM_i \tag{C3}$$

with $F = d\Phi/dr$, the force acting on particles of species i at position $\mathbf{r_i}$. The equation above follows directly from the identity

$$\mathbf{r} \cdot \dot{\mathbf{r}} = -\mathbf{r} \cdot \ddot{\mathbf{r}} + \frac{d}{dt}\ (\mathbf{r} \cdot \dot{\mathbf{r}}) \tag{C4}$$

The last term vanishes when averaged over in an equilibrium system.

In a spherical cluster, with $M(r)$ the mass enclosed within a shell of radius r, the radial force on a unit mass is $F(r) = GM(r)/r^2$, which implies

$$M_i \langle v_i^2 \rangle = \int \frac{GM(r)}{r} dM_i \tag{C5}$$

This is the potential energy which is released during the infall of particles of species i, if we build up the system (gently) from the core outwards. Note that the integrand contains contributions from all species.

If we now define

$$T_i = \frac{1}{2} M_i \langle v_i^2 \rangle \tag{C6}$$

and

$$W_{ij} = \int \frac{GM_j(r)}{r}\ dM_i \tag{C7}$$

we can write

$$2T_i = -\sum_j W_{ij} \tag{C8}$$

where T_i is the kinetic energy of species i and W_{ij} is the energy released during the assembly by particles of species i, due to the attraction of particles j (at a position inside the latest shell of matter being assembled).

The sum of all W_{ij} is the total potential energy:

$$\sum_{ij} W_{ij} = \sum_i \int_0^\infty \frac{G dM_i}{r} \left(\sum_j \int_0^r dM_j \right) = \\ = \frac{1}{2} \sum_{ij} \int_0^\infty \int_0^\infty \frac{G dM_i dM_j}{r} \tag{C9}$$

In the last expression, each term occurs twice, upon exchanging i and j, and therefore the factor 1/2 has been added.

An alternative decomposition of the potential energy is to write

$$E_{pot} = V = \sum_{i \geq j} V_{ij} \tag{C10}$$

where V_{ij} is the potential energy due to the interaction of species i and j. Specifically:

$$V_{ii} = \frac{1}{2} \sum_{ab} \frac{G M_i^2}{r_{ab}} \tag{C11}$$

with a and b running over all particles of species i, and

$$V_{ij} = \sum_{ab} \frac{G m_i m_j}{r_{ab}} \tag{C12}$$

with index a running over particles of species i, and index b over particles of species $j \neq i$.

To avoid the factor $\frac{1}{2}$ in the V_{ii} definition, we can also introduce the symmetric expressions:

$$E_{pot} = U = \sum_{ij} U_{ij} \tag{C13}$$

with

$$U_{ij} = \frac{1}{2} \sum_{ab} \frac{G m_i m_j}{r_{ij}} \tag{C14}$$

In spherically symmetric continuum language:

$$U_{ij} = \frac{1}{2} \int 4\pi \rho_i(r) \, \varphi_j(r) \, dr \tag{C15}$$

Note that the previous W_{ij} can be written in particle language as

$$W_{ij} = \sum_{r_b < r_a} \frac{G m_i m_j}{r_{ab}} \tag{C16}$$

which implies

$$W_{ij} + W_{ji} = U_{ij} + U_{ji} \tag{C17}$$

with $U_{ij} = U_{ji}$, but in general $W_{ij} \neq W_{ji}$

An Example

Consider a thin spherical shell of particles of species 1, each with mass m_1 and total mass $M_1 = N_1 m_1$. The shell has radius r_1. All particles move in circular orbits, with arbitrary orientation of their orbital plane. We can find their velocities in two ways.

First, let us consider a typical particle inside the thin shell. On average, it will feel only half the mass of the shell, namely that part of the shell which is inside the instantaneous location of the particle. Kepler law gives then

$$v_1^2 = \frac{GM_1}{2r_1} \tag{C18}$$

Secondly, we can apply the virial theorem, which reads $2T_1 = -U_{11}$ with

$$T_1 = \frac{1}{2} M_1 \; v_1^2 \tag{C19}$$

and

$$U_{11} = \frac{1}{2} \int_{r_1-\varepsilon}^{r_1+\varepsilon} \rho_1(r) \; 4\pi r^2 \; \{\Phi_1(r) - \Phi_1(\infty)\} \; dr \tag{C20}$$

where 2ε is the thickness of the shell. Since the force in the shell is finite, and the thickness $\varepsilon \to 0$, the potential difference $\Phi(r_1 + \varepsilon) - \Phi(r_1 - \varepsilon) = 0(\varepsilon) \to 0$, and we can write

$$U_{11} = \frac{1}{2} M_1 \cdot \{\Phi_1(r_1) - \Phi_1(\infty)\} = \frac{GM_1^2}{2r_1} \tag{C21}$$

Indeed, the virial theorem gives

$$M_1 v_1^2 = \frac{GM_1^2}{r_1} \tag{C22}$$

in agreement with our first, more intuitive treatment.

Let us now introduce a second shell of matter, of particles of species 2, at radius r_2. Our Kepler orbit argument now gives

$$v_2^2 = \frac{G(M_1 + \frac{1}{2} M_2)}{r_2} \tag{C23}$$

since now the mass M_1 is completely internal for each particle of species 2, whereas only half the mass M_2 is internal, on average, for such a particle. A more careful derivation, using the virial theorem, gives the same result.

Note that the speed of the first shell of particles cannot have been influenced by the assemblage of the second shell, since the force inside a hollow shell is alway zero, even if it contracts or expands. Indeed, in our expressions we see that $v_1 = v_1(M_1,\ r_1)$ and $v_2 = v_2(M_1,\ M_2,\ r_2)$. The interaction between particles of type 1 and 2 increases the velocity of particle 2 only. In our previous notation:

$$
\begin{aligned}
U_{11} = W_{11} &= \frac{GM_1^2}{2r_i} \\
U_{22} = W_{22} &= \frac{GM_2^2}{2r_2} \\
U_{12} = U_{21} &= \frac{GM_1M_2}{2r_2} \\
W_{12} &= 0 \\
W_{21} &= \frac{GM_1M_2}{r_2}
\end{aligned}
\tag{C24}
$$

Indeed, the kinetic energy obeys:

$$
\begin{aligned}
2T_1 = M_1v_1^2 &= \sum_i W_{1i} = W_{11} = \frac{GM_1^2}{2r_1} \\
2T_2 = M_2v_2^2 &= \sum_i W_{2i} = W_{21} + W_{22} = \frac{GM_2^2}{2r_2}(1 + 2\frac{M_1}{M_2})
\end{aligned}
\tag{C25}
$$

FIGURE CAPTIONS

Fig. 1. The density profile of an isothermal gas sphere. r_c is the core radius, defined as being three times larger than the structural length scale (eq. ???). The letters A,B,C indicate fiducial radial positions of an enclosing wall, for a comparison with Fig. 2.

Fig. 2. Relation between energy and temperature for an isothermal gas sphere, plotted in units in which the total mass M, the radius of the enclosing sphere R, and the gravitational constant G are all unity. The letters A,B,C correspond to radial positions of the enclosing wall indicated in Fig. 1.

Fig. 3. Relation between energy and temperature for an isothermal gas sphere, in the approximation of our toy model, as discussed in Appendix A.

Fig. 4. Density profiles in two-component isothermal gas spheres. The ratio μ between the heavy particle mass and the light particle mass is 100, 10, 5, and 2 in Figs. a,b,c, and d, respectively. Each figure is a superposition of six different models, each of which is characterized by a different value of ξ, the ratio of the central densities in the heavy and the light components. The short-dashed line applies to $\xi = 10^8$, the dotted line to $\xi = 10^6$, the short dash–dotted line to $\xi = 10^4$, the long-dashed line to $\xi = 10^2$, the solid line to $\xi = 1$, and the long dash–dotted line to $\xi = 10^{-2}$. For each ξ value, two lines are drawn, for the density $\rho_i(r)$ for each of the two components $i = 1, 2$. The densities are normalized with respect to the central density $\rho_1(0)$ in the light component. The radii are normalized with respect to the core radius r_{c1} of the light particles, defined formally in Eq. (17).

Fig. 5. Shape of the potential well for four different particle mass ratios μ. In each case the central density ratio $\xi = 10$. The potential is given in the dimensionless units introduced in §2.2, while the radial normalization is the same as that used in the previous figure. The full lines indicate the total potential, with the contributions of the light and the heavy particles indicated by the dotted and dashed lines, respectively.

Fig. 6. Energy-temperature diagram for two-component isothermal spheres. For the meaning of the different lines and symbols, see Fig. 4. In Fig. 6b, the letters A,B,C,D correspond to radial positions of the enclosing wall indicated in Fig. 7. In Fig. 6d, we have added one extra line for $\xi = 2.5$, in order to provide insight in the behavior of Fig. 17. In all panels, the normalization of the axes is defined in terms of the total mass M of the system. We have used units in which $G = R = m_1 = k = 1$, for the gravitational constant G, the radius of the wall R, the stellar mass m_1 of the lighter stars, and Boltzmann's constant k.

Fig. 7. Density profiles for the particular two-component isothermal gas sphere defined by a particle mass ratio $\mu = 10$ and a central density ratio $\xi = 10^4$. The letters A,B,C,D indicate fiducial radial positions of an enclosing wall, for a comparison with Fig. 6b. Normalization as in Fig. 4.

Fig. 8. Energy-temperature diagram for two-component isothermal spheres. This figure is similar to Fig. 6a, in that the particle mass ratio is kept constant at $\mu = 100$. However, instead of keeping ξ fixed, we now keep the ratio fixed of the total mass in heavy particles M_2 and that in light particles M_1. Each panel indicates a different value for this ratio, from 10^{-6} in Fig. a till 10^4 in Fig. f.

Fig. 9. As Fig. 8, but for a particle mass ratio of $\mu = 10$.

Fig. 10. As Fig. 8, but for a particle mass ratio of $\mu = 5$.

Fig. 11. As Fig. 8, but for a particle mass ratio of $\mu = 2$.
Fig. 12. Fig. a: Density ratios for our toy-model. Fig. b: Ratio of total masses for our toy model, as a function of half-mass density ratio. Fig. c: Ratio of total masses for our toy model, as a function of central density ratio. Fig. d: Ratio of total masses in the heavy and light components, according to Spitzer's (1987) approximations, as a function of the half-mass density ratio, for three different choices of the parameter α defined in Eq. (47).
Fig. 13. Fig. a: Ratio of total masses in the heavy and light components, as a function of the central density ratio, for our exact solutions in the case of two-component isothermal gas spheres, enclosed in a spherical boundary. This particular case corresponds to a temperature $T_1 = 0.45$ and a particle mass ratio $\mu = 100$. Fig. b: The equivalent curve for the mass ratio between the total heavy mass M_2 and the core mass M_{c1} of the light particles. Fig. c: The half-mass density for the light particles, as a function of central density ratio. Fig. d: The total mass ratio as a function of the half-mass density ratio. Fig. e: The core radius of the lighter mass particles, as a fraction of the radius of the enclosing sphere, as a function of central density ratio. Fig. f: the half-mass density for the heavy particles, as a function of central density ratio.
Fig. 14. As Fig. 13, but for a particle mass ratio of $\mu = 10$.
Fig. 15. As Fig. 13, but for a particle mass ratio of $\mu = 5$.
Fig. 16. As Fig. 13, but for a particle mass ratio of $\mu = 2$.
Fig. 17. As Fig. 16, but for a temperature $T_1/M = 0.49$. For comparison, the results for $T_1/M = 0.45$ are given as dashed lines.

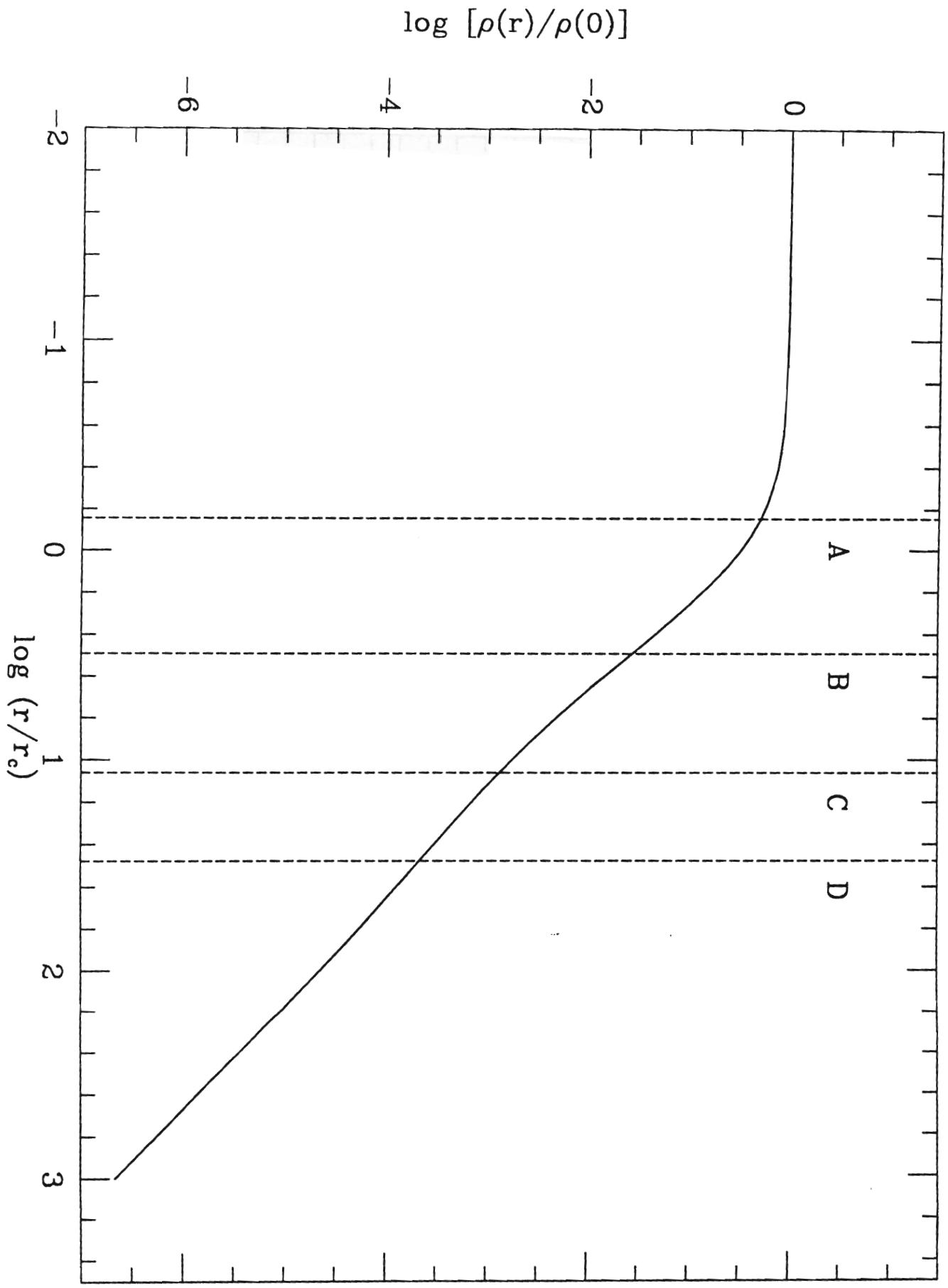

FIGURE 1

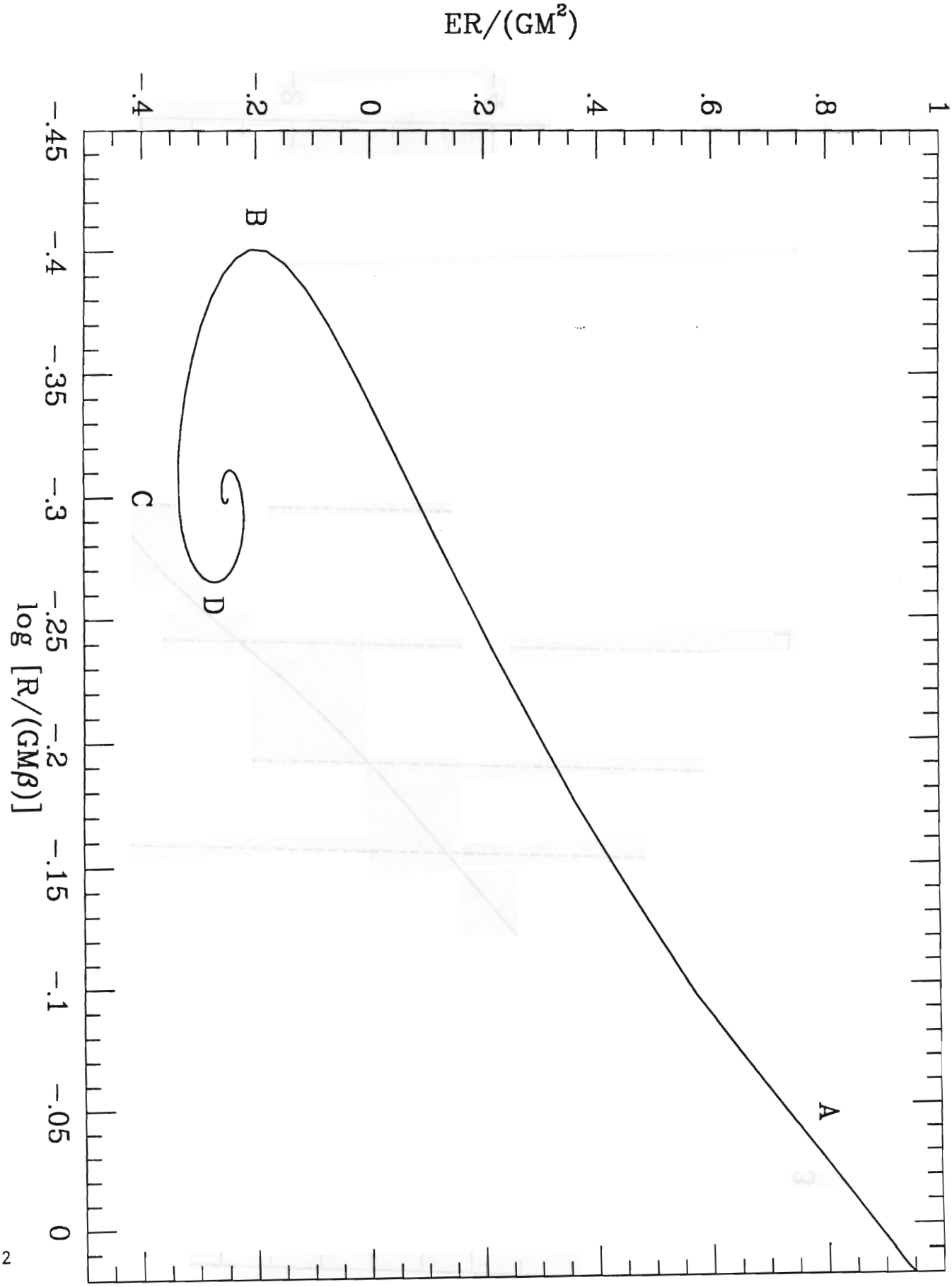

FIGURE 2

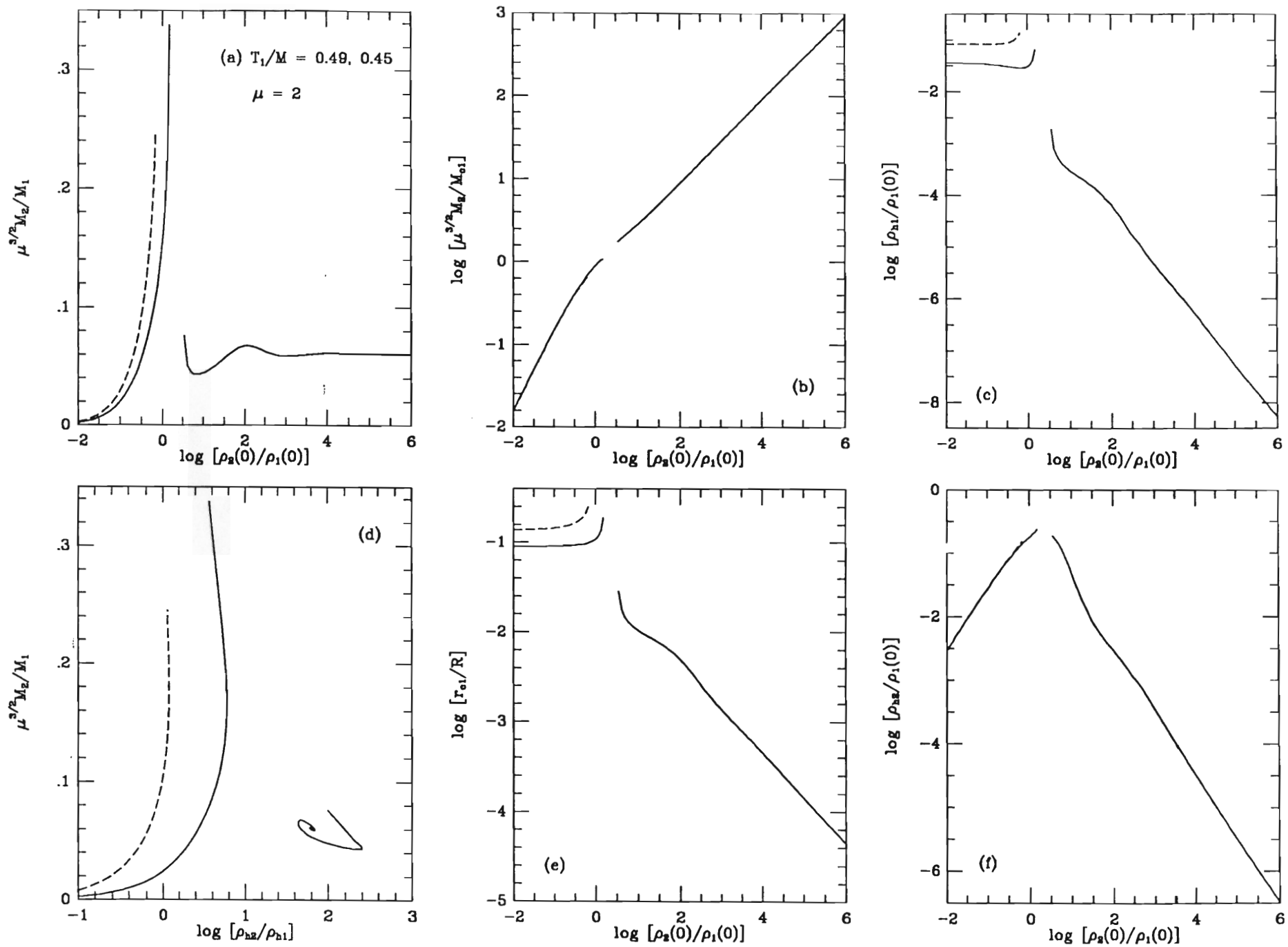
(a) T_1/M = 0.49, 0.45
μ = 2
$\mu^{3/2}M_2/M_1$
log [$\rho_2(0)/\rho_1(0)$]
(b)
log [$\mu^{3/2}M_2/M_{c1}$]
(c)
log [$\rho_{h1}/\rho_1(0)$]
(d)
log [ρ_{h2}/ρ_{h1}]
(e)
log [r_{c1}/R]
(f)
log [$\rho_{h2}/\rho_1(0)$]

Fig. 17

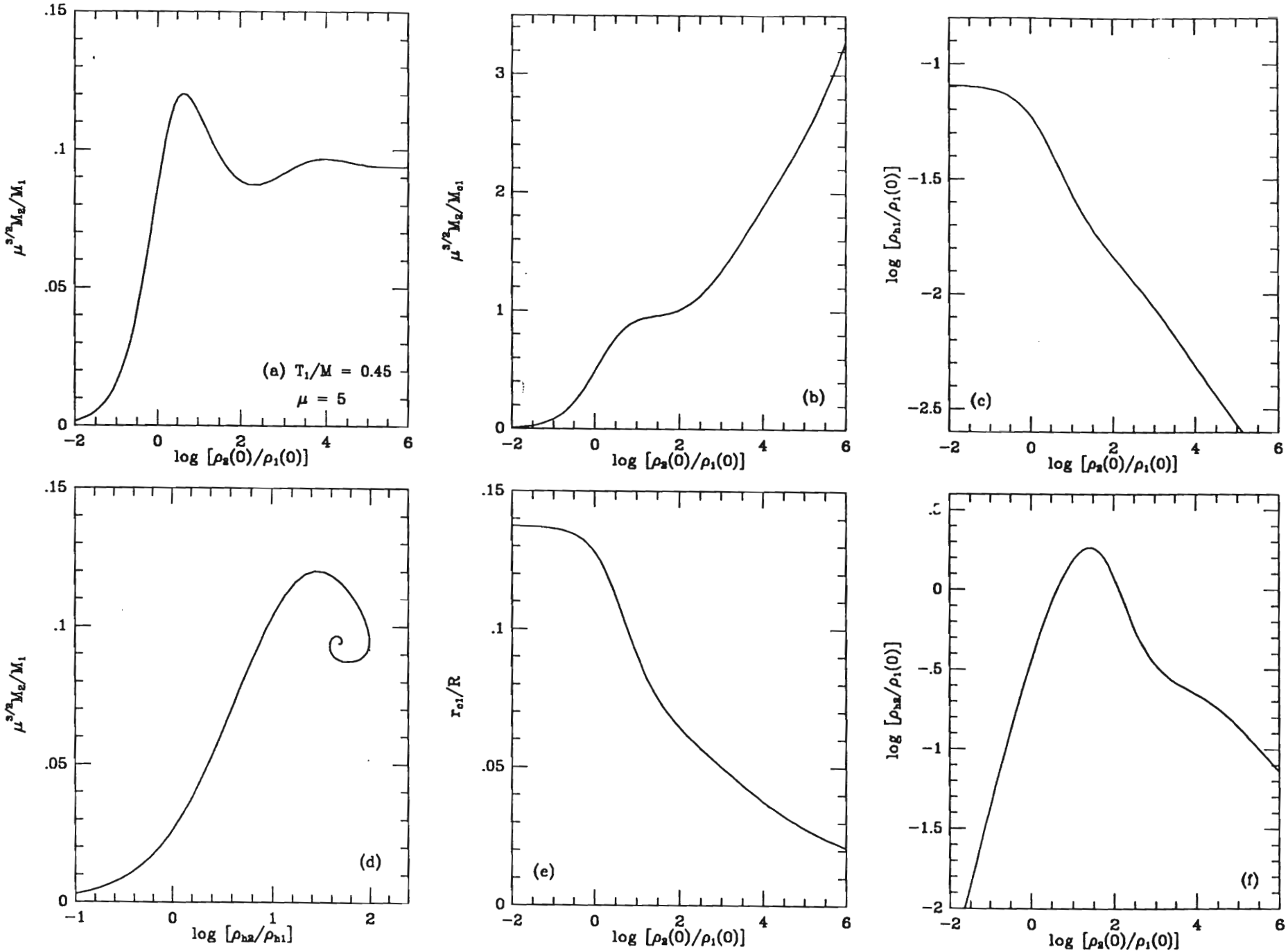
(a) $T_1/M = 0.45$
$\mu = 5$
$\mu^{3/2} M_2/M_1$
$\log [\rho_2(0)/\rho_1(0)]$
(b)
$\mu^{3/2} M_2/M_{c1}$
$\log [\rho_2(0)/\rho_1(0)]$
(c)
$\log [\rho_{h1}/\rho_1(0)]$
$\log [\rho_2(0)/\rho_1(0)]$
(d)
$\mu^{3/2} M_2/M_1$
$\log [\rho_{h2}/\rho_{h1}]$
(e)
r_{c1}/R
$\log [\rho_2(0)/\rho_1(0)]$
(f)
$\log [\rho_{h2}/\rho_1(0)]$
$\log [\rho_2(0)/\rho_1(0)]$

Fig. 16

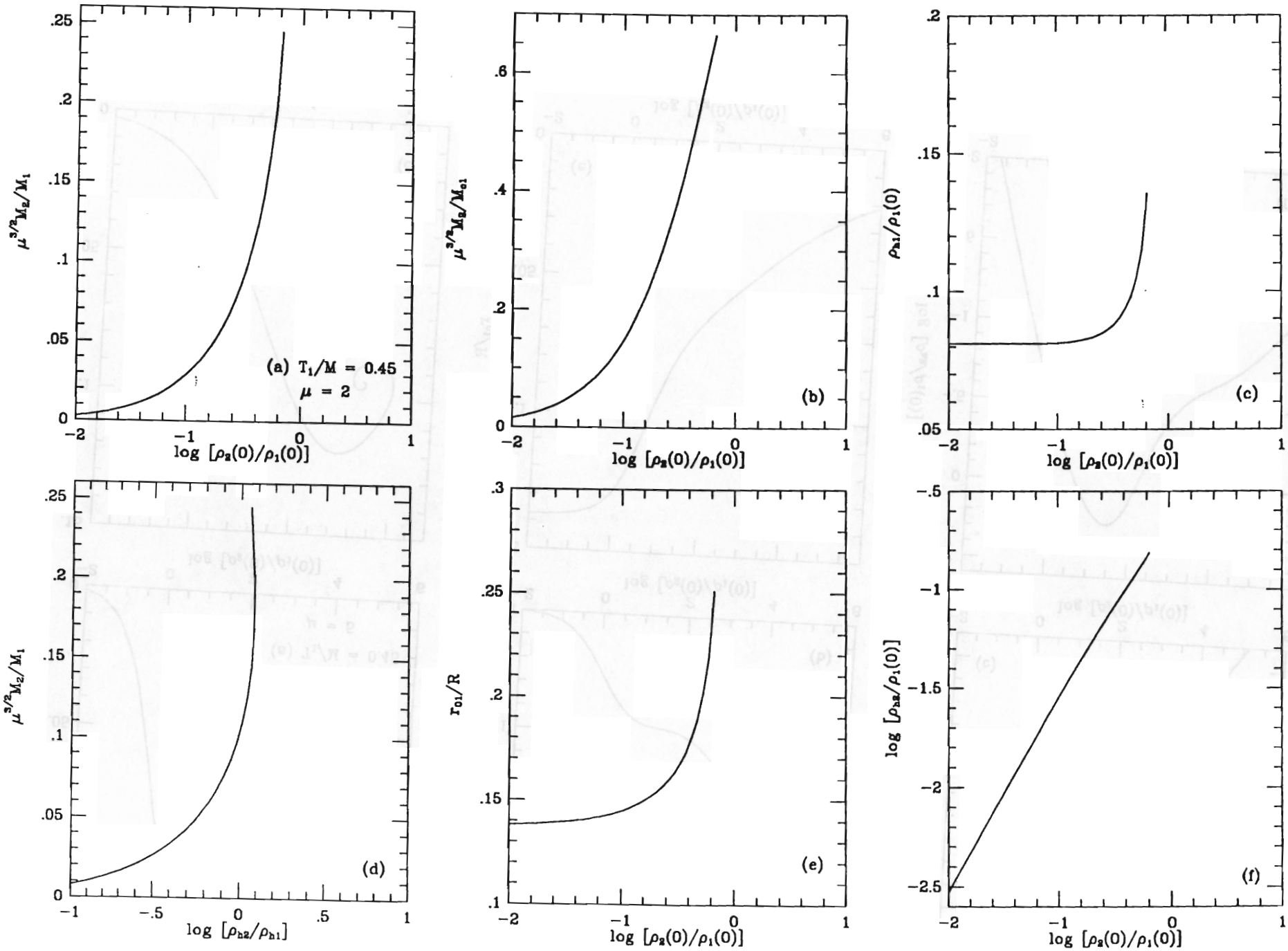
(a) $T_1/M = 0.45$
$\mu = 2$
$\mu^{3/2}M_2/M_1$
$\log\,[\rho_2(0)/\rho_1(0)]$
(b)
$\mu^{3/2}M_2/M_{c1}$
$\log\,[\rho_2(0)/\rho_1(0)]$
(c)
$\rho_{h1}/\rho_1(0)$
$\log\,[\rho_2(0)/\rho_1(0)]$
(d)
$\mu^{3/2}M_2/M_1$
$\log\,[\rho_{h2}/\rho_{h1}]$
(e)
r_{01}/R
$\log\,[\rho_2(0)/\rho_1(0)]$
(f)
$\log\,[\rho_{h2}/\rho_1(0)]$
$\log\,[\rho_2(0)/\rho_1(0)]$

Fig. 15

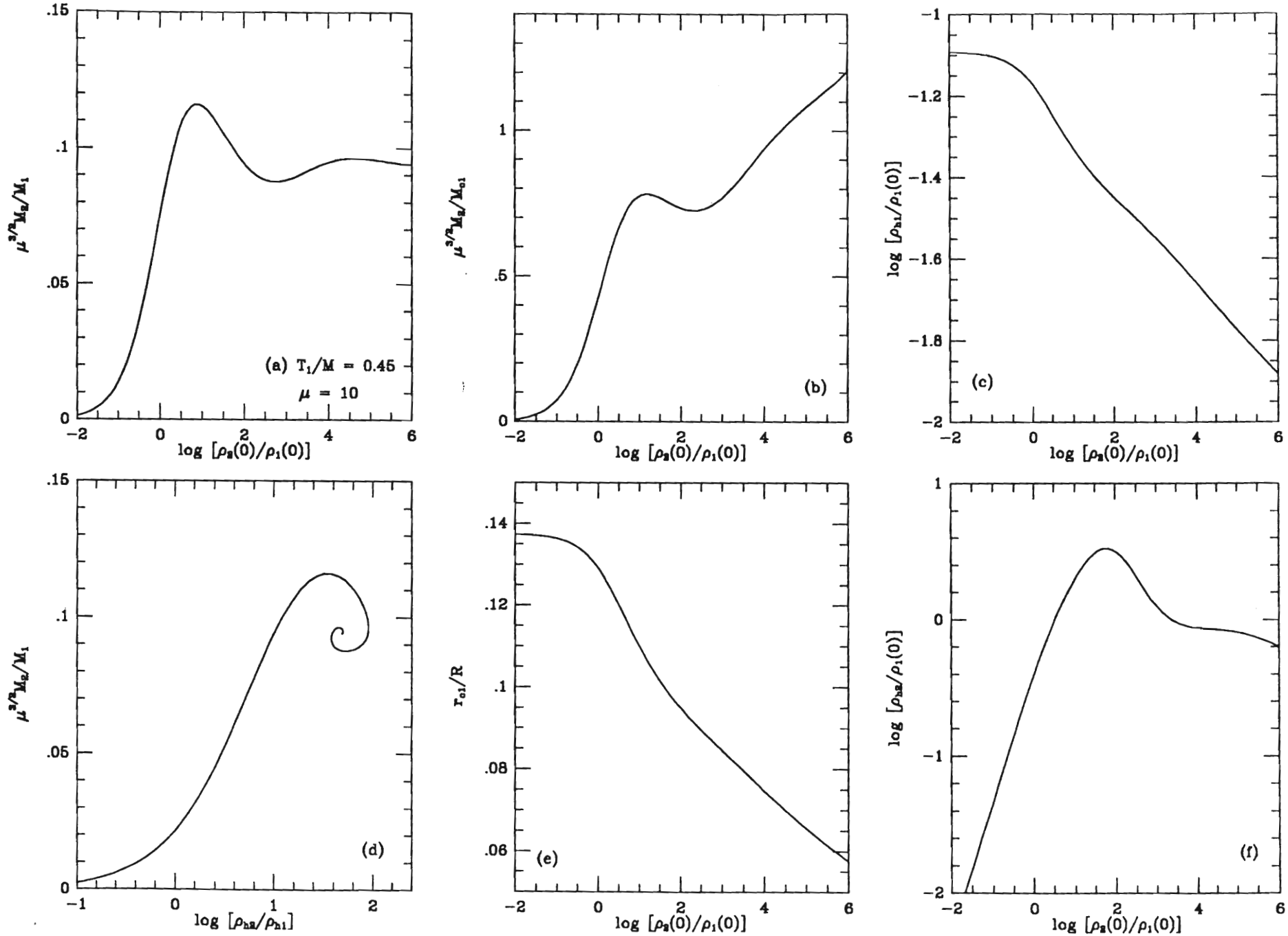
(a) $T_1/M = 0.45$
$\mu = 10$
$\mu^{3/2}M_2/M_1$
$\log[\rho_2(0)/\rho_1(0)]$
(b)
$\mu^{3/2}M_2/M_{c1}$
(c)
$\log[\rho_{h1}/\rho_1(0)]$
(d)
$\log[\rho_{h2}/\rho_{h1}]$
(e)
r_{c1}/R
(f)
$\log[\rho_{h2}/\rho_1(0)]$

Fig. 14

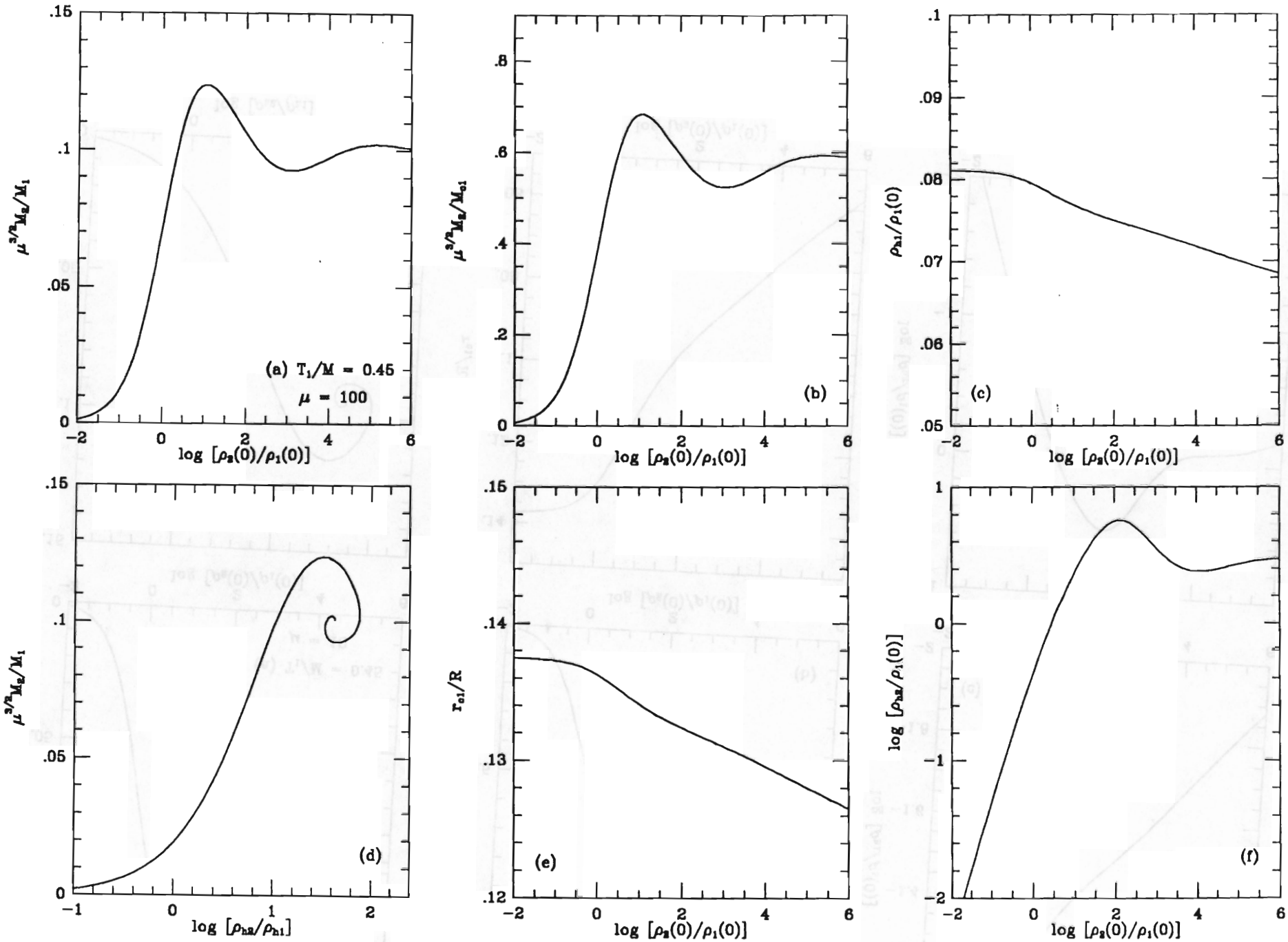
(a) $T_1/M = 0.45$
$\mu = 100$
$\mu^{3/2} M_g/M_1$
$\log [\rho_2(0)/\rho_1(0)]$
(b)
$\mu^{3/2} M_g/M_{c1}$
$\log [\rho_2(0)/\rho_1(0)]$
(c)
$\rho_{h1}/\rho_1(0)$
$\log [\rho_2(0)/\rho_1(0)]$
(d)
$\mu^{3/2} M_g/M_1$
$\log [\rho_{h2}/\rho_{h1}]$
(e)
r_{c1}/R
$\log [\rho_2(0)/\rho_1(0)]$
(f)
$\log [\rho_{h2}/\rho_1(0)]$
$\log [\rho_2(0)/\rho_1(0)]$

Fig. 13

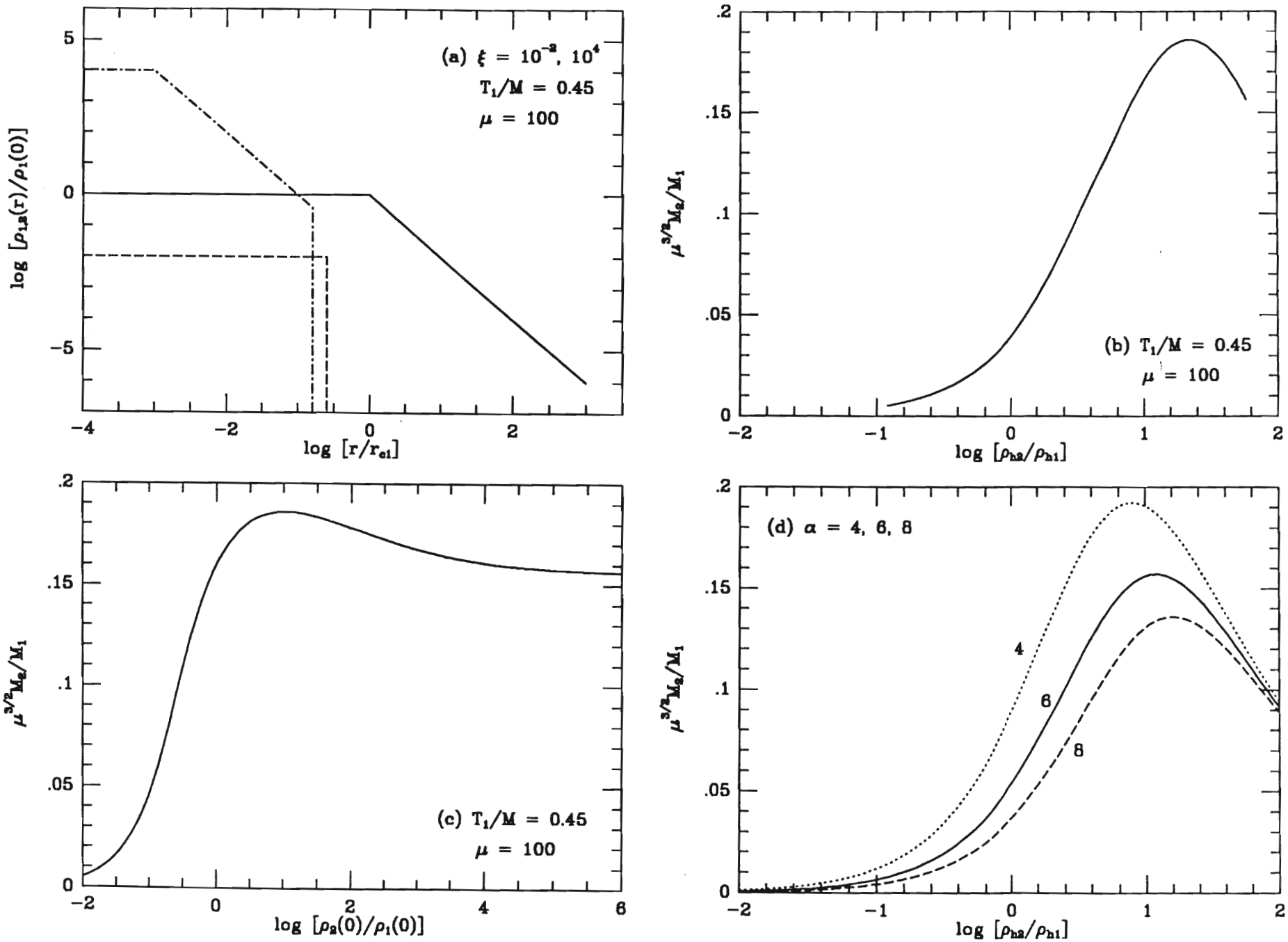
(a) $\xi = 10^{-2}, 10^{4}$
$T_1/M = 0.45$
$\mu = 100$
$\log\,[\rho_{1,2}(r)/\rho_1(0)]$
$\log\,[r/r_{c1}]$
(b) $T_1/M = 0.45$
$\mu = 100$
$\mu^{3/2}M_2/M_1$
$\log\,[\rho_{h2}/\rho_{h1}]$
(c) $T_1/M = 0.45$
$\mu = 100$
$\mu^{3/2}M_2/M_1$
$\log\,[\rho_2(0)/\rho_1(0)]$
(d) $\alpha = 4, 6, 8$
4
6
8
$\mu^{3/2}M_2/M_1$
$\log\,[\rho_{h2}/\rho_{h1}]$

ig. 12

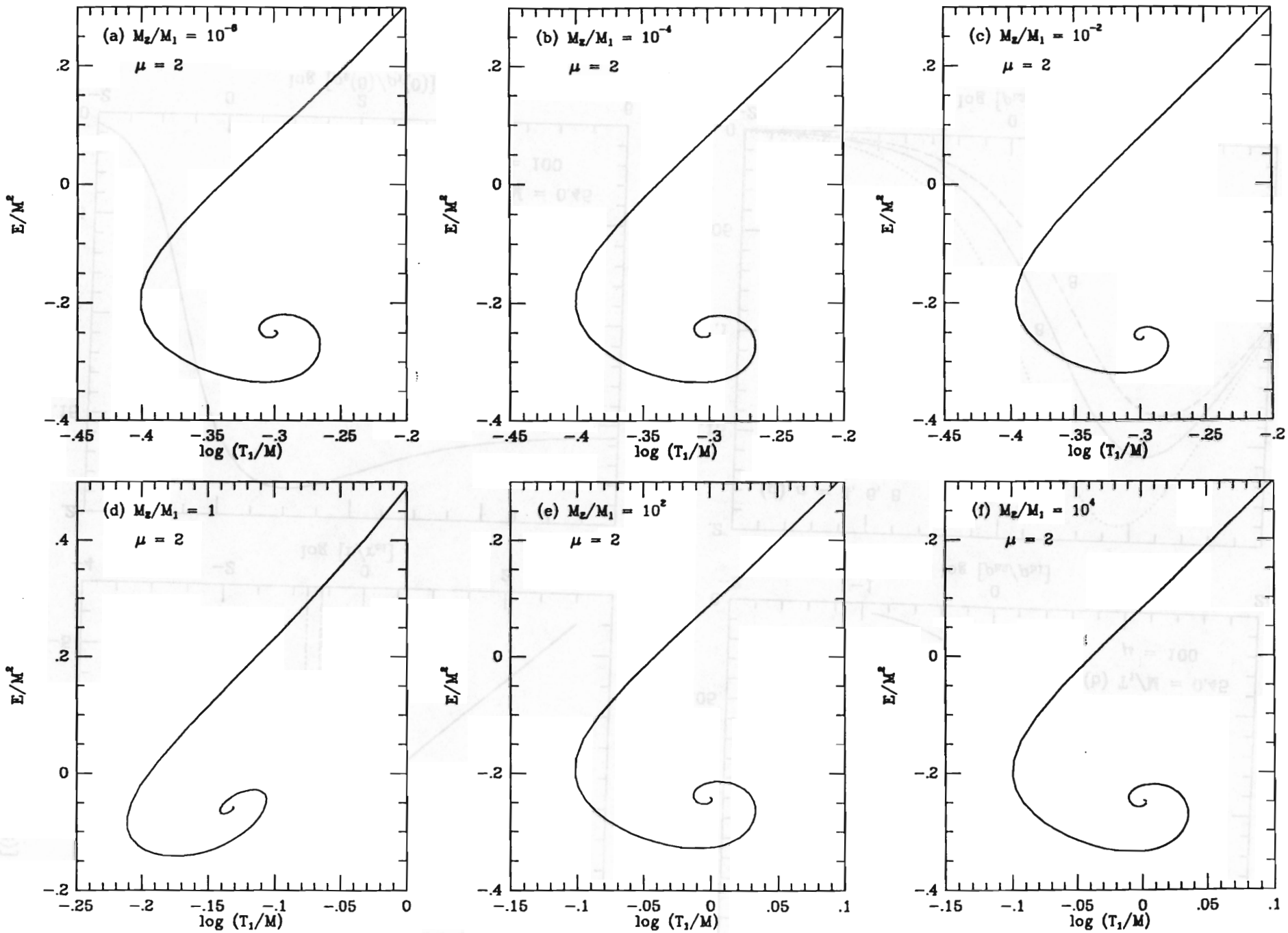
(a) $M_2/M_1 = 10^{-6}$
$\mu = 2$
(b) $M_2/M_1 = 10^{-4}$
$\mu = 2$
(c) $M_2/M_1 = 10^{-2}$
$\mu = 2$
(d) $M_2/M_1 = 1$
$\mu = 2$
(e) $M_2/M_1 = 10^{2}$
$\mu = 2$
(f) $M_2/M_1 = 10^{4}$
$\mu = 2$
E/M^2
$\log (T_1/M)$

Fig. 11

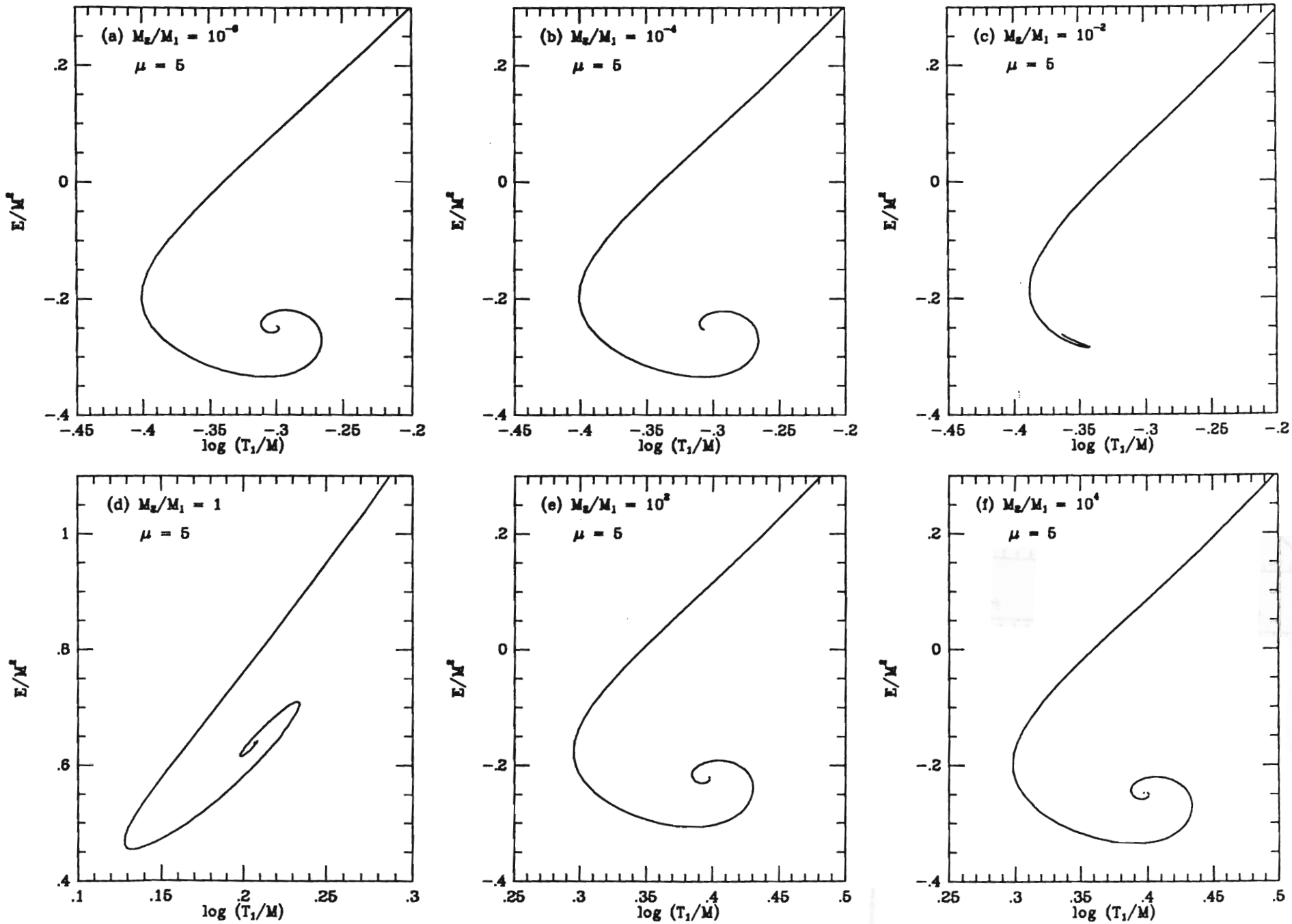
(a) $M_2/M_1 = 10^{-6}$
$\mu = 5$
(b) $M_2/M_1 = 10^{-4}$
$\mu = 5$
(c) $M_2/M_1 = 10^{-2}$
$\mu = 5$
(d) $M_2/M_1 = 1$
$\mu = 5$
(e) $M_2/M_1 = 10^{2}$
$\mu = 5$
(f) $M_2/M_1 = 10^{4}$
$\mu = 5$
E/M^2
$\log (T_1/M)$

Fig. 10

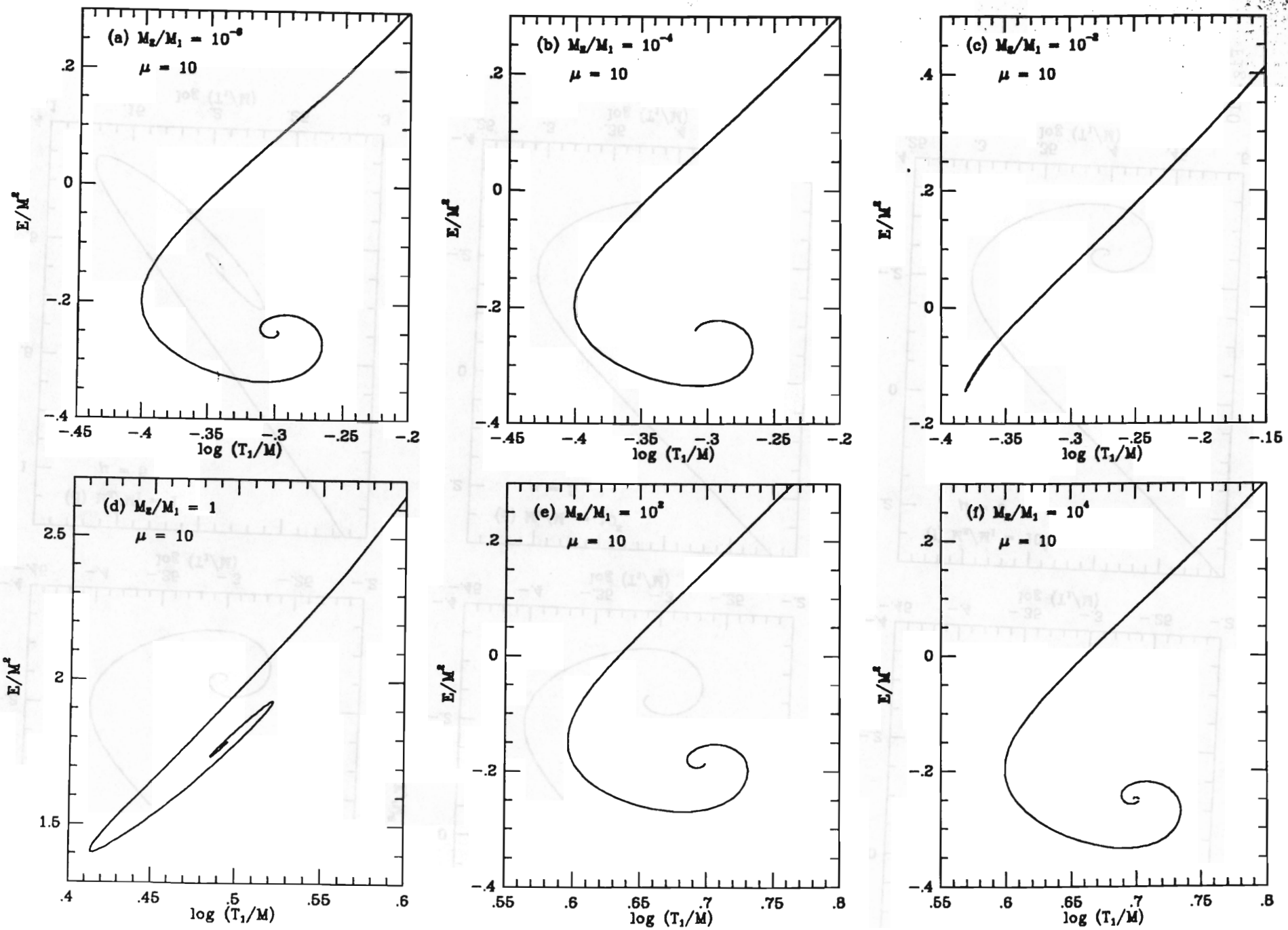
(a) $M_2/M_1 = 10^{-6}$
$\mu = 10$
(b) $M_2/M_1 = 10^{-4}$
$\mu = 10$
(c) $M_2/M_1 = 10^{-2}$
$\mu = 10$
(d) $M_2/M_1 = 1$
$\mu = 10$
(e) $M_2/M_1 = 10^{2}$
$\mu = 10$
(f) $M_2/M_1 = 10^{4}$
$\mu = 10$
E/M^2
$\log (T_1/M)$

Fig. 9

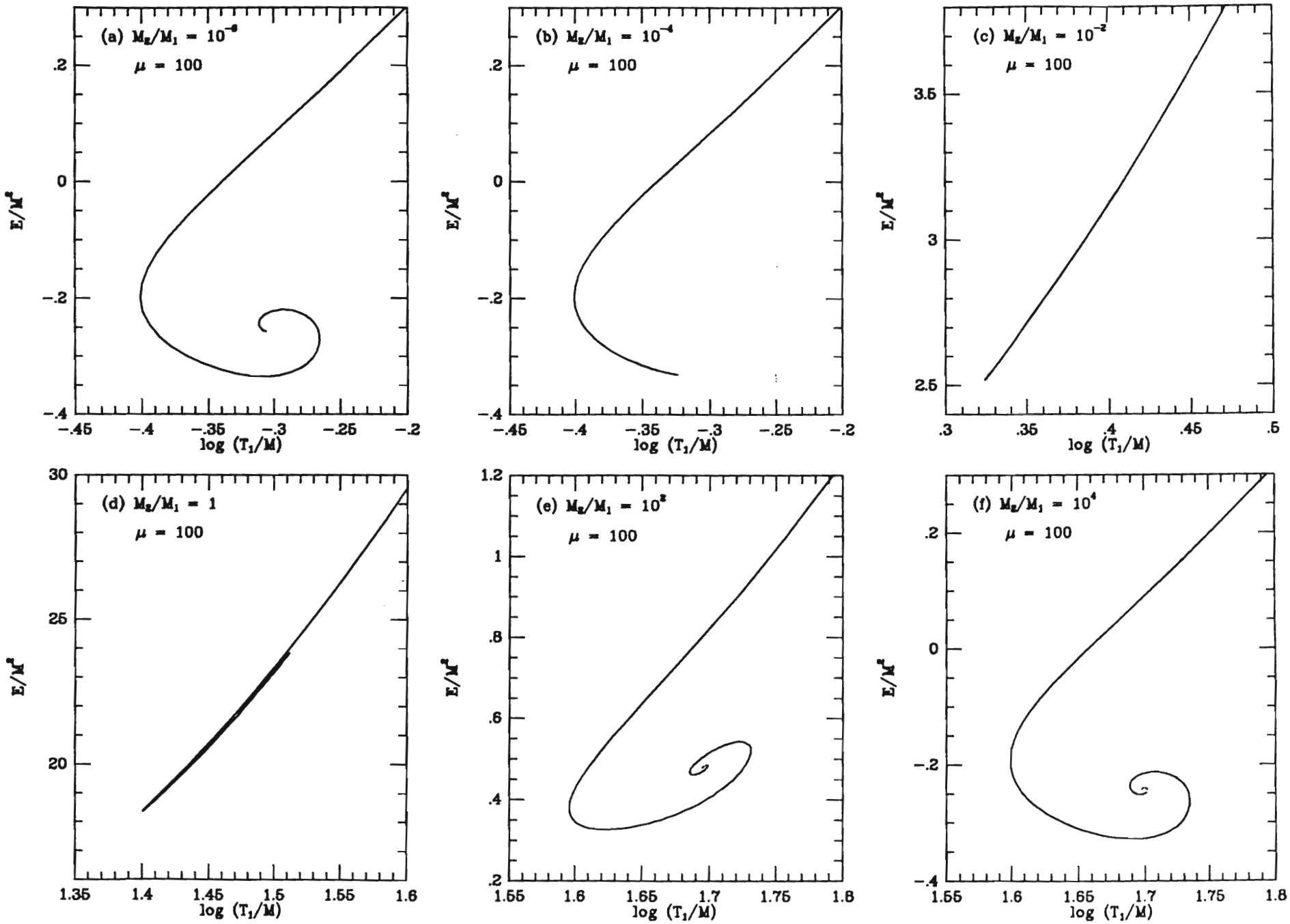
(a) $M_2/M_1 = 10^{-6}$
$\mu = 100$
(b) $M_2/M_1 = 10^{-4}$
$\mu = 100$
(c) $M_2/M_1 = 10^{-2}$
$\mu = 100$
(d) $M_2/M_1 = 1$
$\mu = 100$
(e) $M_2/M_1 = 10^{2}$
$\mu = 100$
(f) $M_2/M_1 = 10^{4}$
$\mu = 100$
E/M^2
$\log (T_1/M)$

Fig. 8

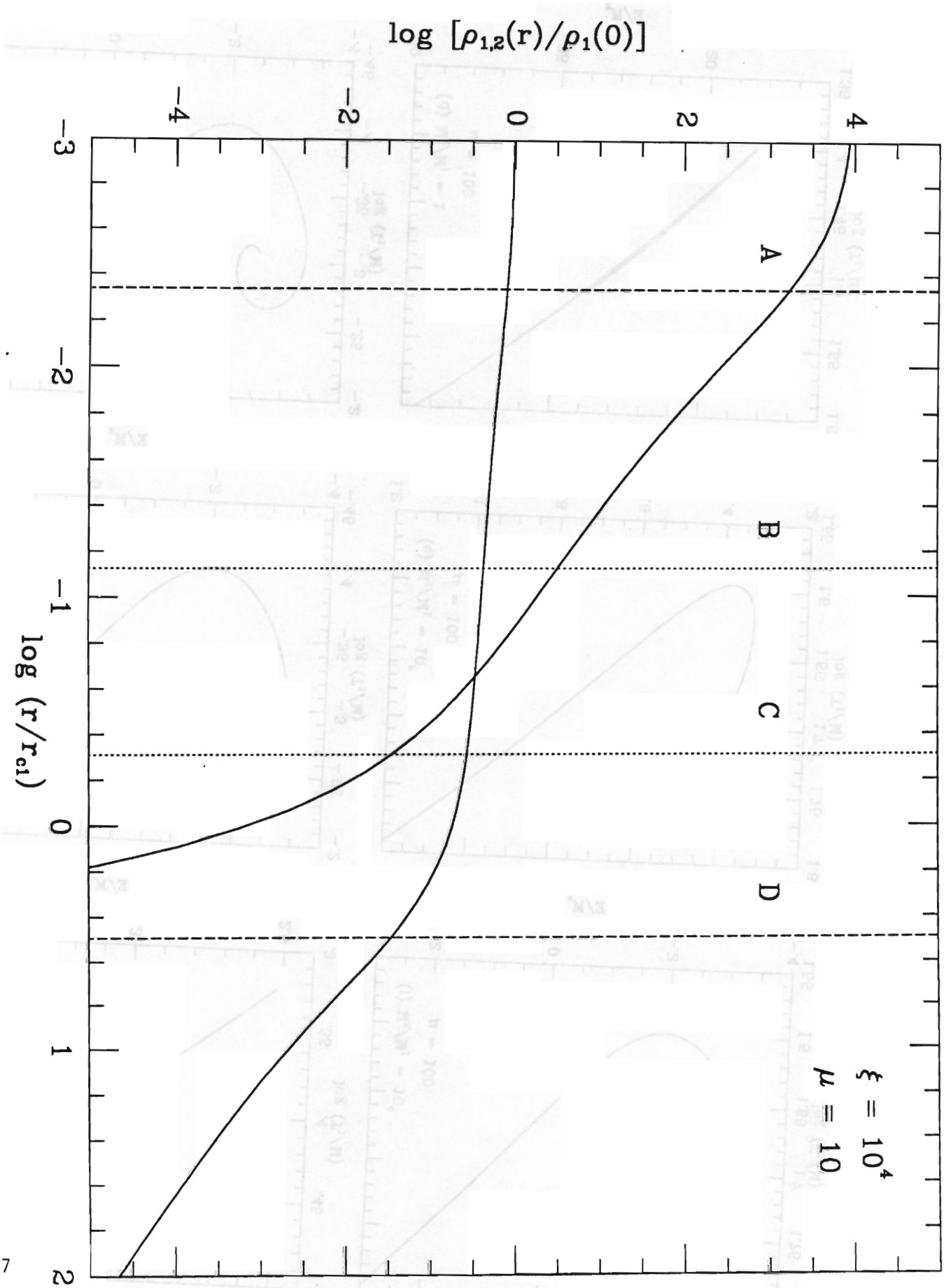

Fig. 7

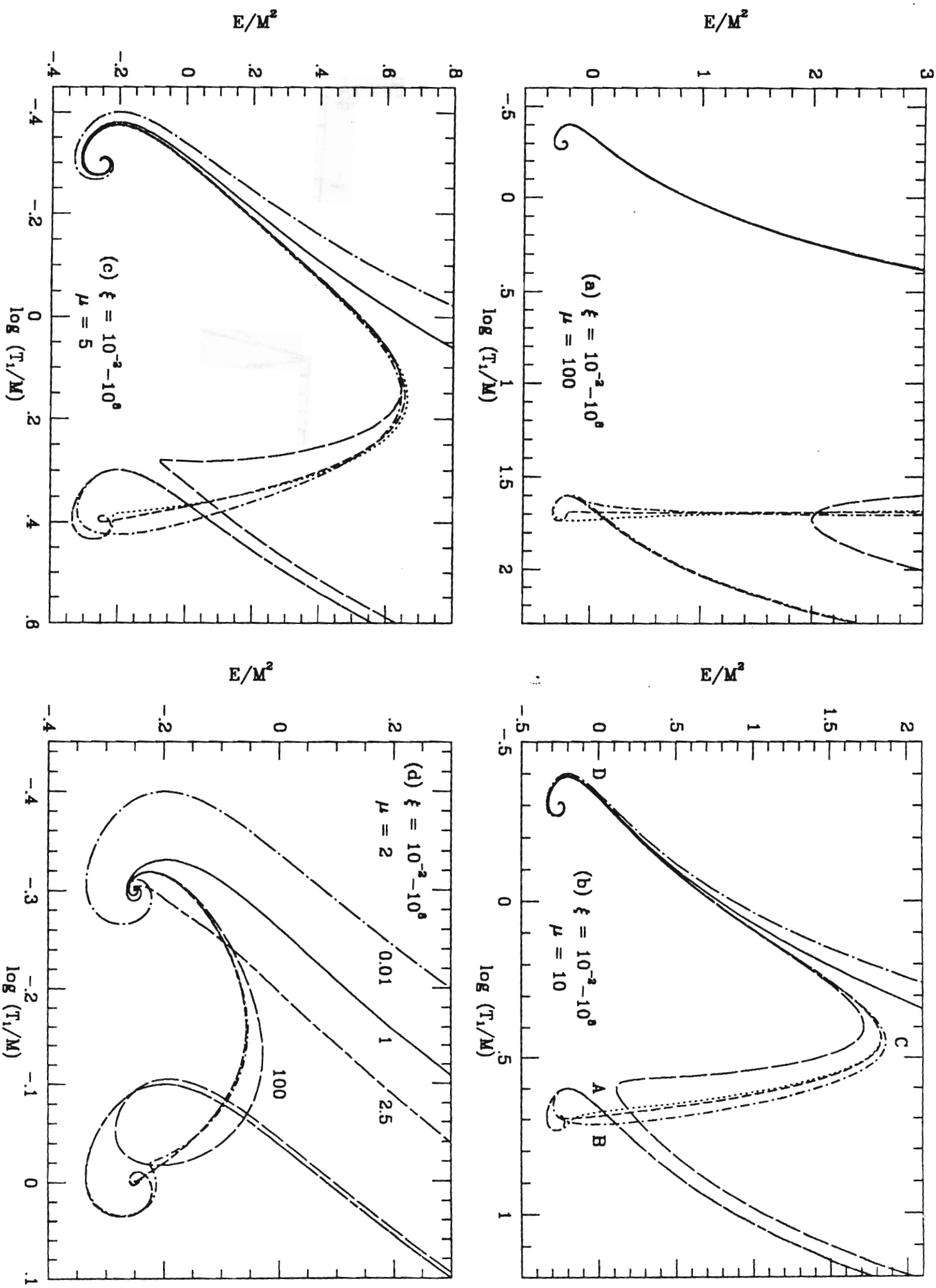
(a) ξ = 10⁻²–10⁸
μ = 100
(b) ξ = 10⁻²–10⁸
μ = 10
(c) ξ = 10⁻²–10⁸
μ = 5
(d) ξ = 10⁻²–10⁸
μ = 2
E/M²
log (T₁/M)
A
B
C
D
0.01
1
2.5
100

Fig. 6

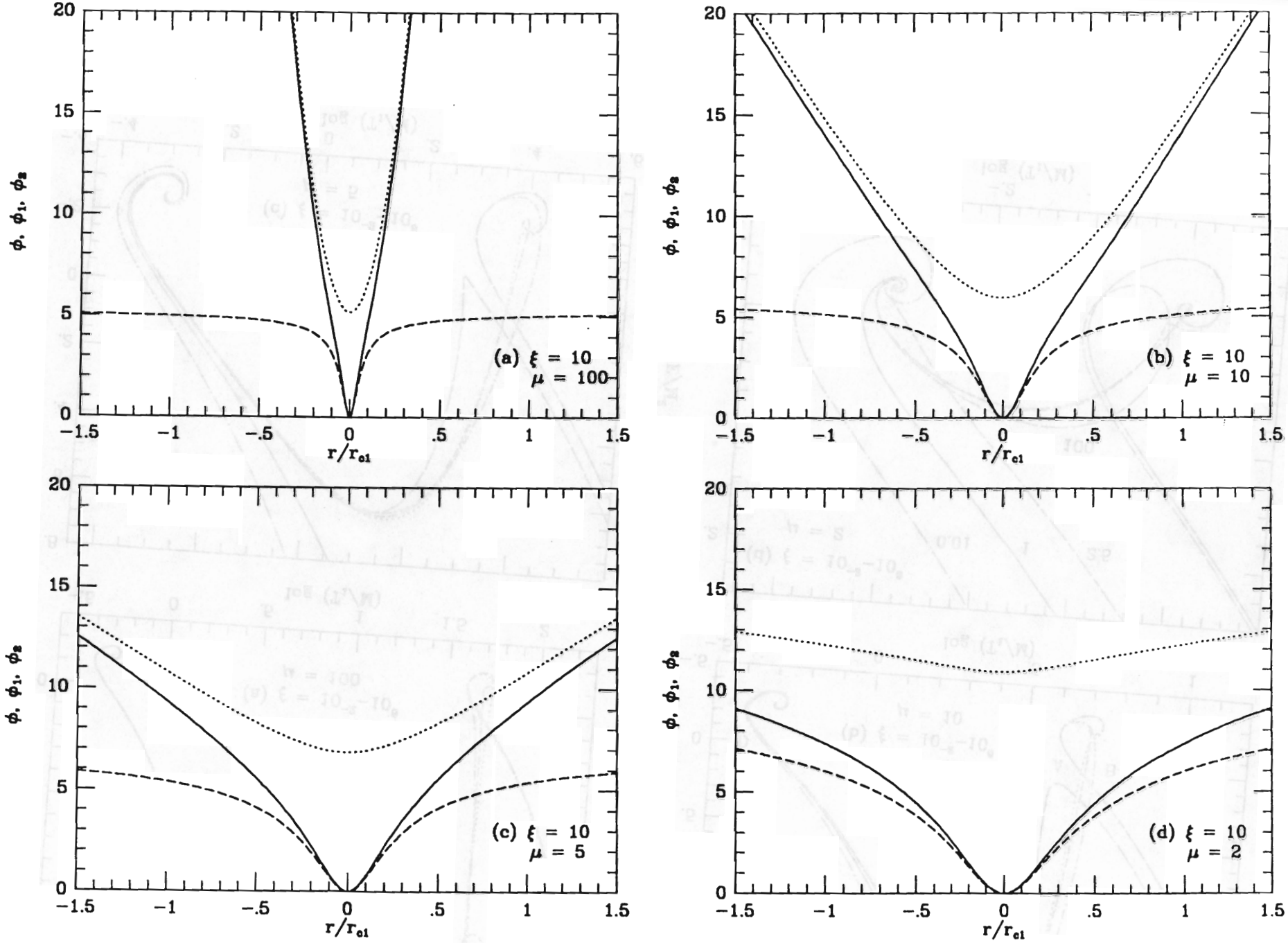
(a) ξ = 10
μ = 100
(b) ξ = 10
μ = 10
(c) ξ = 10
μ = 5
(d) ξ = 10
μ = 2
φ, φ₁, φ₂
r/r_c1
0
5
10
15
20
−1.5
−1
−.5
.5
1
1.5

Fig. 5

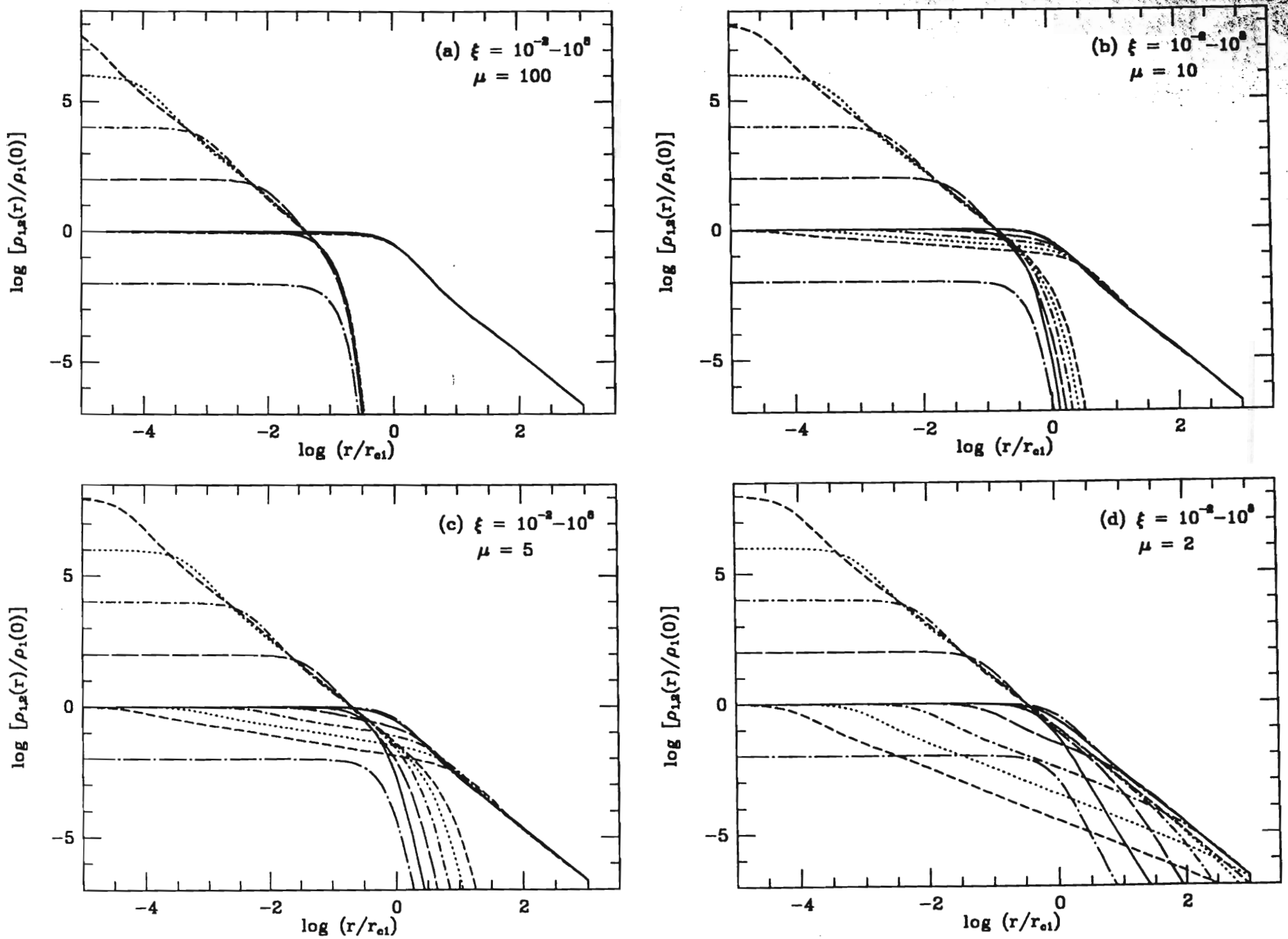
(a) $\xi = 10^{-2}-10^{8}$
$\mu = 100$
(b) $\xi = 10^{-2}-10^{8}$
$\mu = 10$
(c) $\xi = 10^{-2}-10^{8}$
$\mu = 5$
(d) $\xi = 10^{-2}-10^{8}$
$\mu = 2$
$\log\,[\rho_{12}(r)/\rho_1(0)]$
$\log\,(r/r_{c1})$
5
0
−5
−4
−2
0
2

FIG. 4

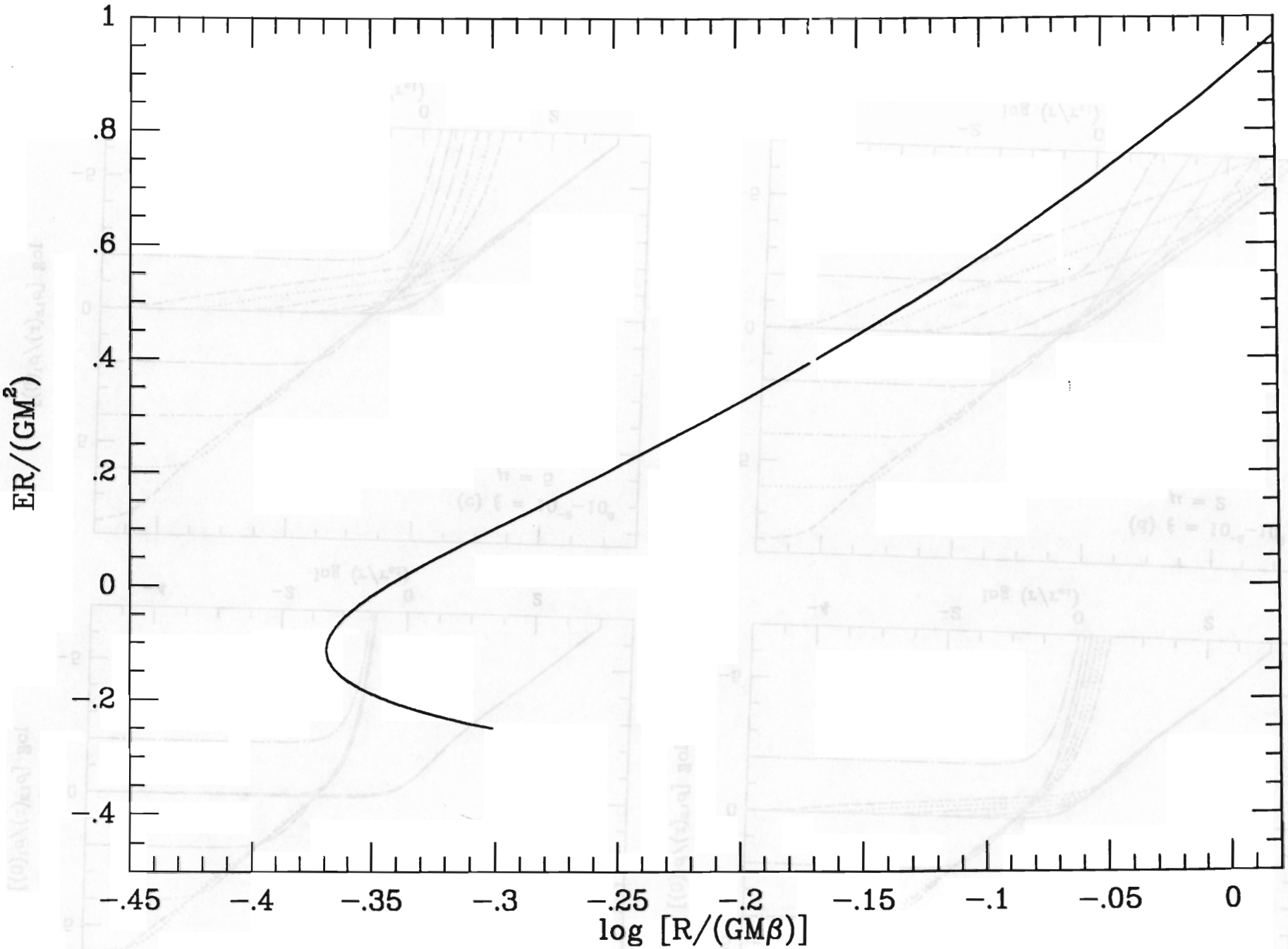

GURE 3